

A CATALOG OF 3MM POINT SOURCES IN THE SAGITTARIUS B2 CLOUD: SIGNS OF EXTENDED STAR FORMATION IN A CENTRAL MOLECULAR ZONE CLOUD

ADAM GINSBURG^{1,2}

¹ *Jansky fellow of the National Radio Astronomy Observatory, Socorro, NM 87801 USA*

² *European Southern Observatory, Karl-Schwarzschild-Straße 2, D-85748 Garching bei München, Germany*

ABSTRACT

We report ALMA observations at 3 mm of the extended Sgr B2 cloud. We detected 263 compact sources, the majority of which have extents smaller than 5000 AU. By ruling out alternative possibilities such as externally ionized globules, we conclude that these sources are predominantly protostars or centrally condensed prestellar cores. The spatial distribution of these sources, which is spread over a $\sim 12 \times 3$ pc region, demonstrates that Sgr B2 is experiencing a highly extended star formation event, not just an isolated ‘starburst’ within the protocluster regions Main (M), North (N), and South (S). While all of the detected protostars reside in regions of high column density, not all regions of high column density ($N(\text{H}_2) > 10^{23} \text{ cm}^{-2}$) contain a high density of protostars. **We observe a threshold** for high-mass star formation that is substantially higher than the solar vicinity threshold for star formation, implying either that high-mass star formation requires a higher column density or that the star formation threshold in the CMZ is higher than the solar vicinity threshold. These observations constitute the largest known single, possibly coeval to within 1 Myr, sample of forming massive stars.

This version produced Wednesday 21st June, 2017 at 23:39.

1. INTRODUCTION

The Central Molecular Zone (CMZ) of our Galaxy appears to be overall deficient in star formation relative to the gas mass it contains (Longmore et al. 2013; Kauffmann et al. 2016a,b; Barnes et al. 2016, 2017). This deficiency suggests that star formation laws, i.e., the empirical relations between the star formation rate and gas column density, are not universal. The gas conditions in the Galactic center are different from those in nearby clouds, providing a powerful lever arm in a few parameters (e.g., pressure, temperature, velocity dispersion; Kruijssen & Longmore 2013; Ginsburg et al. 2016; Immer et al. 2016; Shetty et al. 2012; Henshaw et al. 2016) to assess the influence of environmental effects on star formation.

The observations that have demonstrated the star formation deficiency compare bulk tracers of star formation to > 0.1 pc resolution gas observations (e.g. Barnes et al. 2017). More recently, high-resolution observations of selected clouds in the CMZ have revealed very few star-forming cores even when examined at high resolution and sensitivity (Rathborne et al. 2014, 2015; Kauffmann et al. 2016a,b). There are few sites with obvious signs of ongoing star formation along the CMZ dust ridge. The Sgr B2 N (North), M (Main), and S (South) protoclusters (Schmiedeke et al. 2016, Figure 1) are actively forming star clusters and contain high-mass protostars and many compact H II regions (e.g. Higuchi et al. 2015; Gaume et al. 1995). Besides Sgr B2, at a much lower level, the 20 km s $^{-1}$ and 50 km s $^{-1}$ clouds (Lu et al. 2016; ?), and Clouds C, D, and E (Ginsburg et al. 2015; Barnes et al. 2017, Walker et al, in prep.). These regions contain a handful of high-mass cores but only a small number of protostars and no ultra- or hyper-compact H II regions.

We report the first observations of extended, ongoing star formation in a Galactic center cloud *not* isolated to a centralized protocluster dust clump. We observed a $\sim 15 \times 15$ pc section of the Sgr B2 cloud and identified star formation along the entire molecular dust ridge known as Sgr B2 Deep South (DS, also known as the ‘Southern Complex’ Jones et al. 2012; Schmiedeke et al. 2016). These observations allow us to perform the first star-counting based determination of the star formation rate within the dense molecular gas of the CMZ.

We adopt a distance to Sgr B2 $D_{\text{SgrB2}} = 8.4$ kpc, which is consistent with Sgr B2 being located in the CMZ dust ridge. While Reid et al. (2009) measure a closer distance of 7.9 kpc, we use a value closer to the IAU-recommended Galactic Center distance of 8.5 kpc, accounting for the distance difference of ≈ 100 pc measured by Reid et al. (2009). Choosing the closer distance

would result in masses and luminosities smaller by 12%, which would not affect any of the conclusions of this paper.

We describe the observations in Section 2. In this paper, we focus on the continuum sources, which we identify in Section 3.1. We classify the sources in Section 3.2. **TODO: complete this ‘overview of the paper’ once all sections have been included.**

2. OBSERVATION AND DATA REDUCTION

2.1. ALMA data

Data were acquired as part of ALMA project 2013.1.00269.S (see Table 1). Observations were taken in ALMA Band 3 with the 12m Total Power array (not included in this work), the ALMA 7m array, and in two configurations with the ALMA 12m array. The setup included the maximum allowed number of channels, 30720, across 4 spectral windows in a single polarization; the single-polarization mode was adopted to support moderate spectral resolution (~ 0.8 km s $^{-1}$, 244 kHz channels) across the broad bandwidth. The basebands were centered at 89.48, 91.28, 101.37, and 103.23 GHz with bandwidth 1.875 GHz (total 7.5 GHz).

The ALMA QA2 calibrated measurement sets were combined to make a single high-resolution, high-dynamic range data set. We imaged the continuum jointly across all four basebands (without excluding any spectral line regions), and found that the central regions surrounding Sgr B2 M were severely affected by artifacts that could not be cleaned out. We therefore ran 3 iterations of phase-only self-calibration and two iterations of amplitude + phase self-calibration, the latter using multi-scale multi-frequency synthesis with two Taylor terms (Rau & Cornwell 2011), to yield a substantially improved image (see Appendix B). The total dynamic range, measured as the peak brightness in Sgr B2 to the RMS noise in a signal-free region of the combined 7m+12m image, is 18000 (noise ~ 0.09 mJy/beam, 0.05 K), while the dynamic range within one primary beam ($\sim 0.5''$) of Sgr B2M is only 5300 (noise ~ 0.3 mJy/beam, 0.16 K). Because of the dynamic range limitations and an empirical determination that clean did not converge if allowed to go too deep, we cleaned to a threshold of 0.1 mJy/beam over all pixels with $S_\nu > 2.5$ mJy / beam as determined from a previous iteration. The final image used for most of the analysis in this paper was imaged with Briggs robust parameter 0.5, achieving a beam size $0.54'' \times 0.46''$.

We also produced cubes of all of the spectral lines. These were lightly cleaned with a maximum of 2000 iterations of cleaning to a threshold of 100 mJy/beam. The noise is typically ≈ 9 mJy beam $^{-1}$ (6 K) per

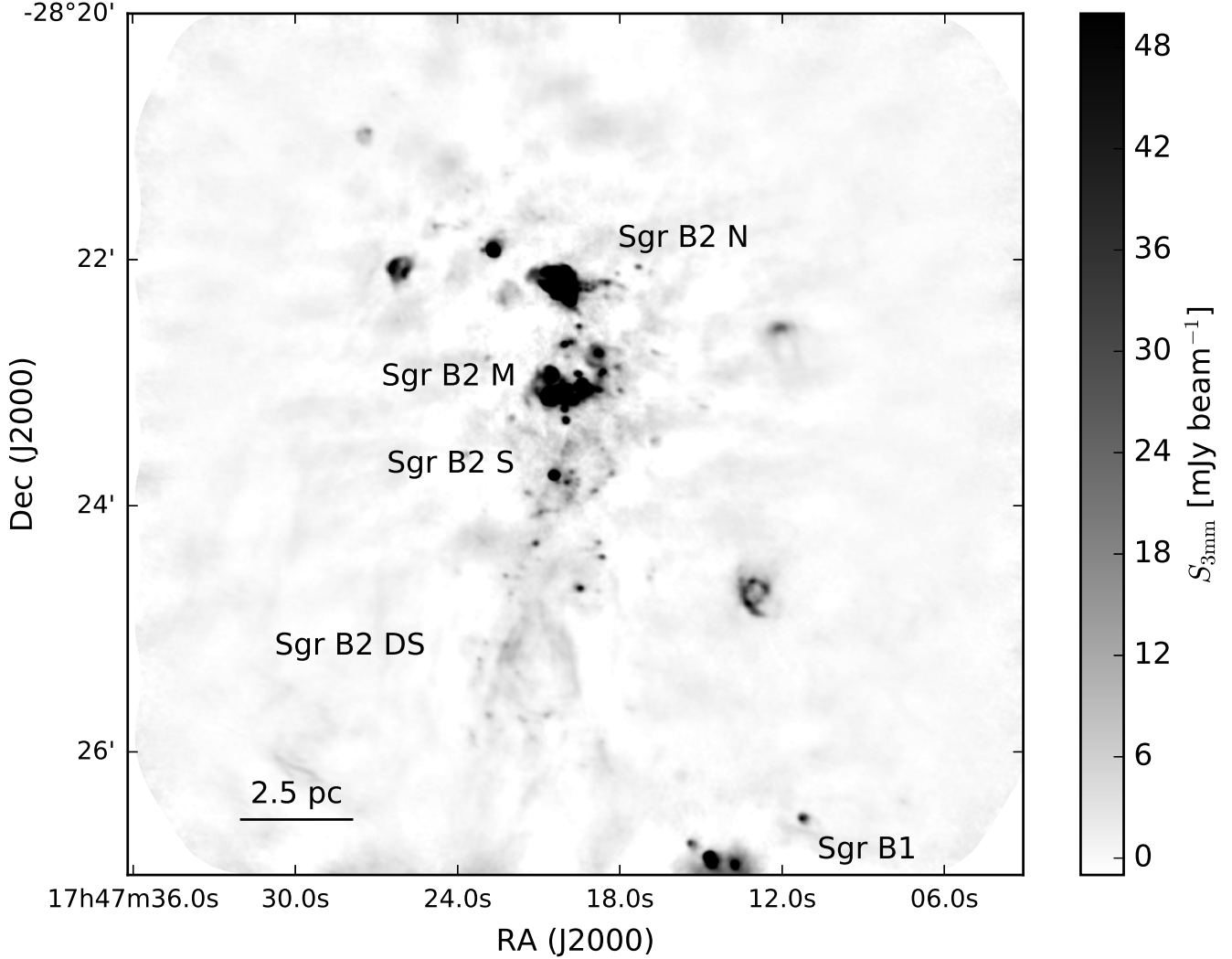


Figure 1. An overview of the Sgr B2 region, with the most prominent clusters labeled. The image shows the ALMA 3 mm observations imaged with $1.5''$ resolution to emphasize the larger scale emission features. For a cartoon version of this figure, see Schmiedeke et al. (2016) Figure 1.

Table 1. Observation Summary

Date	Array	Total Observing Time	Longest Baseline Length
		seconds	meters
01-Jul-2014	7m	4045	49
02-Jul-2014	7m	4043	49
03-Jul-2014	7m	7345	48
06-Dec-2014	12m	6849	349
01-Apr-2015	12m	3464	328
02-Apr-2015	12m	3517	328
01-Jul-2015	12m	3517	1574
02-Jul-2015	12m	10598	1574

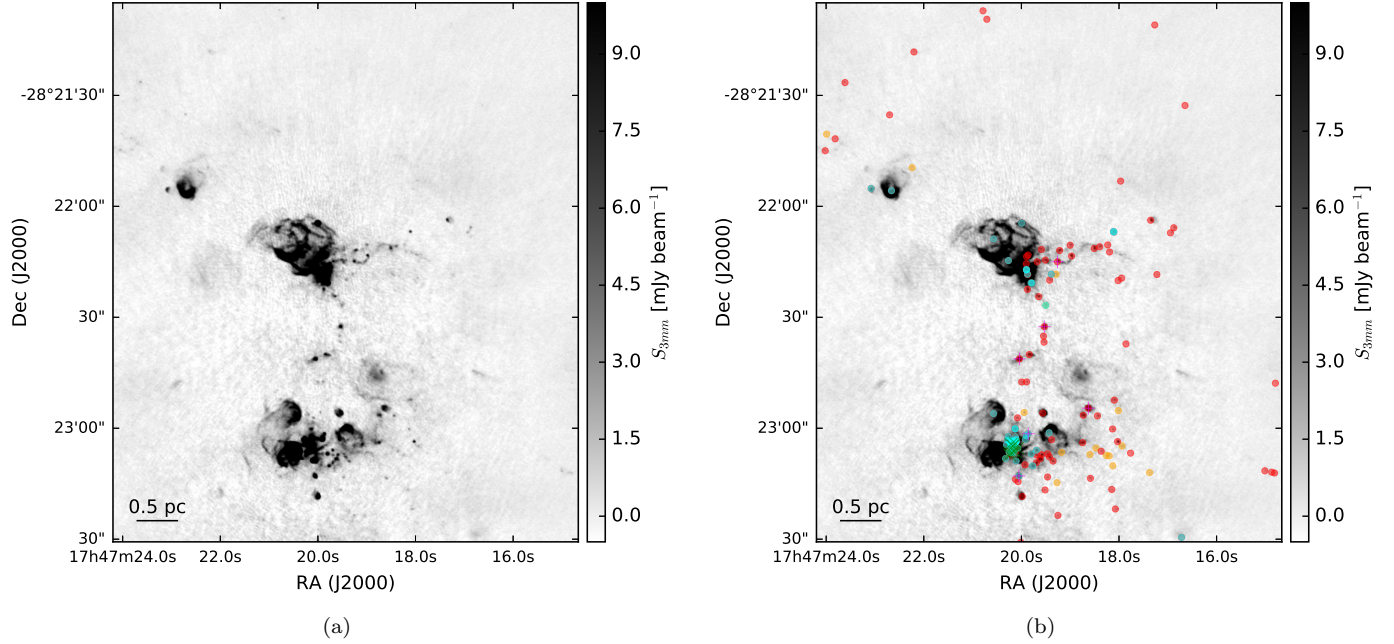


Figure 2. Images of the ALMA 3 mm continuum in the Sgr B2 M and N region. The right figure additionally includes markers at the position of each identified continuum pointlike source: red dots are ‘conservative’, high-confidence sources, orange dots are ‘optimistic’, low-confidence sources, cyan are H II regions, magenta +’s are masers, and green X’s are X-ray sources. The massive protocluster Sgr B2 M is the collection of H II regions and compact sources in the lower half of the image. The other massive protocluster, Sgr B2 N, is in the center. Imaging artifacts (sidelobes) are evident at the 1-2 mJy bm^{-1} level. The crowded parts of the images are shown with inset zoom-in panels in Figure 3.

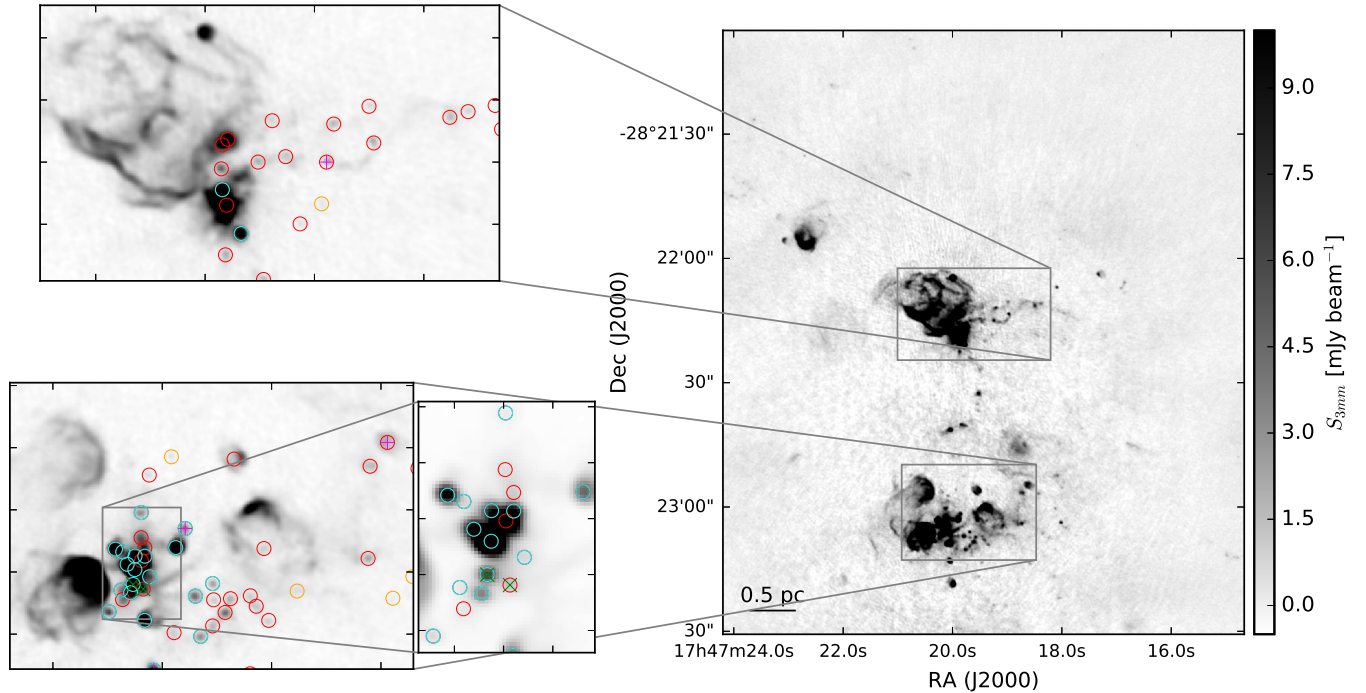


Figure 3. A close-in look at the Sgr B2 M and N region. Multiple insets show identified sources in some of the richer sub-regions. The points are colored as in Figure 2. The background image is the ALMA 3 mm continuum.

0.8 km s⁻¹ channel in the robust 0.5 cubes. No self-calibration was applied, both because the dynamic range limitations were less significant and because the image cubes are computationally expensive to process. Before continuum subtraction, dynamic range related artifacts similar to those in the continuum images were present, but these structures are identical across frequencies, and were therefore removable in the image domain. We use median-subtracted cubes for the majority of our analysis, noting that the only location in which an error > 5% on the median-estimated continuum is expected is the Sgr B2 North core (Sanchez-Monge et al. 2017, Sanchez-Monge et al. 2017, submitted). While many lines were included in the spectral setup, only HC₃N J=10-9 is discussed here; of the included lines, it is the brightest and most widely detected.

The processed data are available from http://apps.canfar.net/storage/list/SgrB2_ALMA_3mm in the form of four ~ 225 GB data cubes. Additional data sets will be made available via dataverse or some other service prior to submission.

2.2. Other data - Column Density Maps

We use archival data to create column density maps. To determine the column density and dust temperature on large angular scales, we use Herschel Hi-Gal data (Molinari et al. 2010) to perform SED fits to each pixel (Battersby et al, in prep.). These fits were performed at 25'' resolution, using the 70, 160, 250, and 350 μm data and excluding the 500 μm channel. The estimated uncertainty is $\sim 25\%$, with an upper limit on the systematic uncertainty of a factor of two (Batterby et al, in prep.).

The CSO SHARC data were reported in Bally et al. (2010) and have a nominal resolution of 9'' at 350 μm , however, at this resolution, the SHARC data display a much higher surface brightness than the Herschel data on the same angular scale. An assumed resolution of 11.5'' gives a better surface brightness match and is consistent with the measured scale of Sgr B2 N in the image. This calibration difference is likely to have been a combination of blurring by pointing errors, surface imperfections, the gridding process, and flux calibration errors. In any case, the Herschel data provide the most trustworthy absolute calibration scale, since they were taken from space and calibrated to an absolute scale using Planck data (Bendo et al. 2013; ?).

The JCMT SCUBA 450 μm data were reported in Pierce-Price et al. (2000) and Di Francesco et al. (2008) with a resolution of 8''. We found that the SCUBA data had a flux scale significantly discrepant from the Herschel-SPIRE 500 μm data, even accounting for the

central wavelength difference. We had to scale the SCUBA data up by a factor ≈ 3.0 to make the data agree with the Herschel-SPIRE images on the angular scales they are both hypothetically sensitive to. While such a large flux calibration error seems implausible, the measured FWHM toward Sgr B2 N is approximately 14'', which means the beam area is $\approx 3\times$ larger than the theoretical size. We attempted to fit several other isolated sources in the large SCUBA map, and the smallest FWHM we measured was $\approx 10.5''$. Between the larger beam area, flux calibration errors (quoted at 20% in Pierce-Price et al. 2000), and the dust emissivity correction (35-50% for $\beta = 3-4$), this large flux scaling factor is plausible. This large correction factor is consistent with the large error beam found by Di Francesco et al. (2008), with effective FWHM $\approx 17.3''$, since they used additional smoothing when creating their maps.

To obtain higher resolution column density maps, we used the combined Herschel-SPIRE+SHARC and Herschel-SPIRE+SCUBA maps. We created several column density maps, some assuming arbitrary constant temperatures equal to the minimum and maximum expected dust temperatures (20 and 50 K), and another using the temperature measured with Herschel interpolated onto the higher-resolution SCUBA and SHARC grids. Because of the interpolation and fixed temperature assumptions, the column maps are not very accurate and should not be used for systematic statistical analysis of the column density distribution (i.e., PDF analysis) without careful attention to the large implied uncertainties. However, these higher-resolution data are used in this paper to provide the best estimates of the local column density around our sample of compact millimeter continuum sources. The data combination is discussed in more detail in Appendix A.

3. ANALYSIS

3.1. Continuum Source Identification

We selected compact continuum sources by eye, scanning across images with different weighting schemes (different robust parameters). An automated selection is not viable across the majority of the field because there are many extended H II regions that dominate the overall map emission. A future automated selection algorithm may work if images at comparable resolution at other frequencies become available; the H II-region sources could then be excluded. Additionally, however, there are substantial imaging artifacts produced by the extremely bright emission sources in Sgr B2 M ($S_{3mm,max} \approx 1.6$ Jy) and Sgr B2 N ($S_{3mm,max} \approx 0.3$ Jy) that make automated source identification particularly challenging in

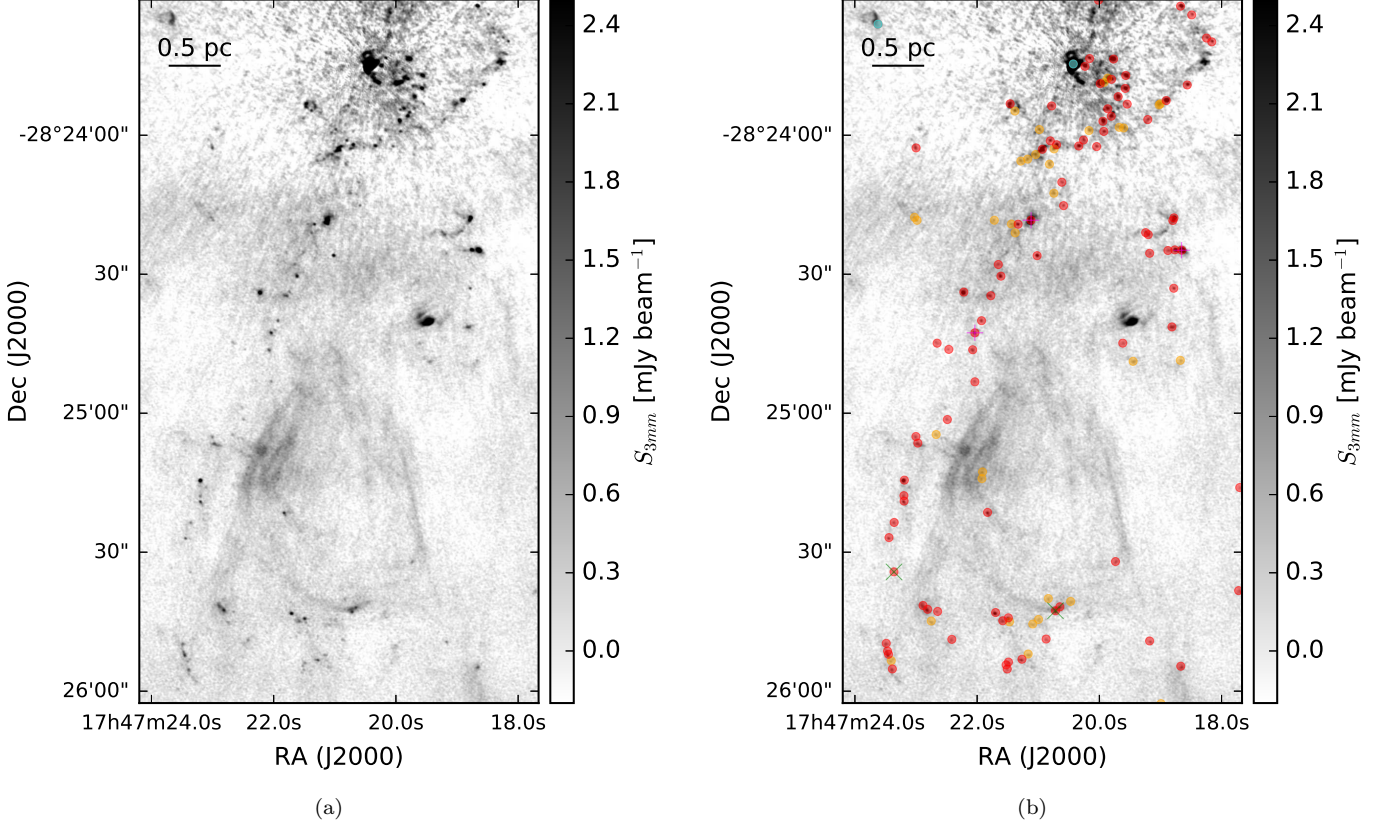


Figure 4. Images of the ALMA 3 mm continuum in the Sgr B2 Deep South (DS) region. The right figure additionally includes markers at the position of each identified continuum pointlike source: red dots are ‘conservative’, high-confidence sources, orange dots are ‘optimistic’, low-confidence sources, cyan are H II regions, magenta +’s are masers, and green X’s are X-ray sources. The H II region Sgr B2 S is the bright source at the top of the image; imaging artifacts can be seen surrounding it. The largest angular scales are noisier than the small scales; the $\sim 20''$ -wide east-west ridge at around $-28:24:30$ is likely to be an imaging artifact. By contrast, the diffuse components in the southern half of the image are likely to be real. The crowded parts of the images are shown with inset zoom-in panels in Figure 5.

the most source-dense regions. All of these features are evident in Figures 2 and 4.

Because the noise varies significantly across the map (it is higher near Sgr B2 M), a uniform selection criterion is not possible. We therefore include two levels of source identification, ‘high confidence’ sources, which are selected conservatively in regions of low-background, and ‘low-confidence’ sources that are somewhat lower signal-to-noise and are often in regions with higher background (labeled ‘conservative’ and ‘optimistic’, respectively, in Figure 6 and 7). Both of these selection criteria are significantly more conservative than a local $5-\sigma$ threshold.

We measure the local noise for each source by taking the median absolute deviation in an annulus 0.5 to $1.5''$ around the source center. All but 7 sources have signal-to-local-noise ratios $S/N > 7$. These sources are all in regions of particularly high background or source density and therefore have overestimated local noise.

Our selection criteria result in a reliable but potentially incomplete catalog. The greatest concerns for our completeness are in the densest regions around Sgr B2 M and N. In these regions, dynamic range limitations increase the background noise and make fainter sources difficult to detect, as described in Section 2. Additionally, they both contain extended structures, including H II regions and dust filaments, which likely obscure compact sources.

Outside of the dense clusters, every locally $5-\sigma$ peak was visually inspected. Peaks that were part of extended structures but not significantly different from them (e.g., a $5-\sigma$ peak sitting on a $4-\sigma$ extended structure) were excluded. We excluded sources with extents $r > 1''$, i.e., extended H II regions.

For a subset of the sources, primarily the brightest, we measured the spectral index α based on CASA `tclean`’s 2-term Taylor expansion model of the data (parameters `deconvolver='mtmfs'` and `nterms=2`). This measure-

ment is over a narrow frequency range (≈ 90 – 100 GHz). `tclen` produces α and $\sigma(\alpha)$ (error on α) maps, and we used the α value at the position of peak intensity for each source. We include in the analysis only those sources with $|\alpha| > 5\sigma(\alpha)$ or $\sigma(\alpha) < 0.1$; the latter include sources with $\alpha \sim 0$ measured at relatively high precision. Sixty sources met these criteria. Several of the brightest sources did not have significant measurements of α because they are in the immediate neighborhood of Sgr B2 M or N and therefore have significantly higher background and noise, preventing a clear measurement. To check the calibration of the spectral index measurement, we imaged one of our calibrators, J1752-2956, and obtained a spectral index $\alpha = -0.62 \pm 0.14$, consistent with the expected $\alpha \approx -0.7$ for an optically thin synchrotron source (e.g. Condon & Ransom 2007). We also note that the *relative* spectral index measurements in our catalog should be accurate, since all sources come from the same map with identical calibration.

We detected 263 compact continuum sources, and they are listed in Table ?? **This ref is broken and I don't know why yet..** Their flux distribution is shown in Figure 6. The distribution of their measured spectral indices α is shown in Figure 7. Generally, spectral indices $\alpha < 0$ indicate nonthermal (e.g., synchrotron) emission, $-0.1 < \alpha < 2$ may correspond to free-free sources of various optical depths, $\alpha = 2$ for any optically thick thermal source, and $\alpha > 2$ usually indicates optically thin dust emission. These indices will be discussed further in the next Section.

3.2. Source Classification

For the majority of the detected sources, we have only a continuum detection at 3 mm. In this section, we employ a variety of arguments to classify the sample of new sources. For the majority of the detected sources, we have no detections at other band to assist with the classification, so we discuss what types of objects they could be given their 3 mm continuum detections. Plausible emission mechanisms include free-free and thermal dust emission, so we explore whether the sources could be different classes free-free sources in subsections 3.2.1, 3.2.2, and 3.2.3. We conclude that they are primarily dusty sources in subsection 3.2.4.

We visually inspected the spectra extracted from the full line cubes, and no lines are detected peaking toward the majority of the sources (most sources have emission in some lines, but this emission is clearly extended and not associated with the compact source). Given the relatively poor line sensitivity (RMS ≈ 6 K), the dearth of detections is not very surprising. We therefore cannot use spectral lines to classify most sources.

A subset of the detected sources have detections at other bands and can be classified based on previous literature work, especially those associated with H II regions detected at 0.7 and 1.3 cm (Gaume et al. 1995; Mehringer et al. 1995; De Pree et al. 1996, 2015). We classified sources as H II regions if there is a corresponding 0.7 or 1.3 cm source from one of the previous VLA surveys within one ALMA beam ($0.5''$). 23 of our sources are classified as H II regions. The majority of these are unresolved, but we have included H II regions with radii up to $\approx 1''$ in our catalog. Optically thick H II regions (like any blackbody) have a spectral index $\alpha = 2$. Optically thin H II regions have a nearly flat spectral index, $\alpha = -0.1$ (Condon & Ransom 2007). The observed sources with H II region counterparts have spectral indices consistent with the theoretical expectation for optically thin H II regions in Figure 7. The existing VLA data do not cover the entire area of our observations, so we only have a lower limit on the number of H II regions in our sample; the sources in Sgr B2 DS have not yet been observed in the radio at high resolution.

We note some properties of dust at 3 mm. At 8.4 kpc, a 1 mJy source corresponds to an optically thin gas mass¹ of $M(40K) = 18 M_{\odot}$ or $M(20K) = 38 M_{\odot}$ assuming a dust opacity index $\beta = 1.75$ ($\alpha = 3.75$ on the Rayleigh-Jeans tail) to extrapolate the Ossenkopf & Henning (1994) opacity to $\kappa_{3mm} = 0.0018 \text{ cm}^2 \text{ g}^{-1}$ (per gram of gas). Our dust-only (i.e., excluding free-free emission) 5- σ sensitivity limit at 20 K therefore ranges from $M > 19 M_{\odot}$ (0.5 mJy) to $M > 94 M_{\odot}$ (2.5 mJy) across the map. If we were to assume that these are all cold, dusty sources, as is typically (and reasonably) assumed for local clouds, they would be extremely massive and dense, with the lowest measurable density being $n(20K) > 1 \times 10^8 \text{ cm}^{-3}$ (corresponding to $19 M_{\odot}$ in an $r = 0.2'' = 1700 \text{ AU}$ radius sphere). Such extreme objects are possible, but since we have detected > 100 of these sources, we evaluate other possibilities.

We start with a few alternatives we are able to rule out: externally ionized gas globules, internally ionized H II regions from an older generation of ‘interloper’ stars, and internally ionized H II regions from a newly-formed generation of massive stars. We then discuss why these sources are most likely embedded protostars.

3.2.1. Alternative 1: The sources are externally ionized gas blobs

One possibility is that these sources are not dust-dominated, nor pre- or protostellar, but are instead ex-

¹We assume a gas-to-dust ratio of 100 throughout this work.

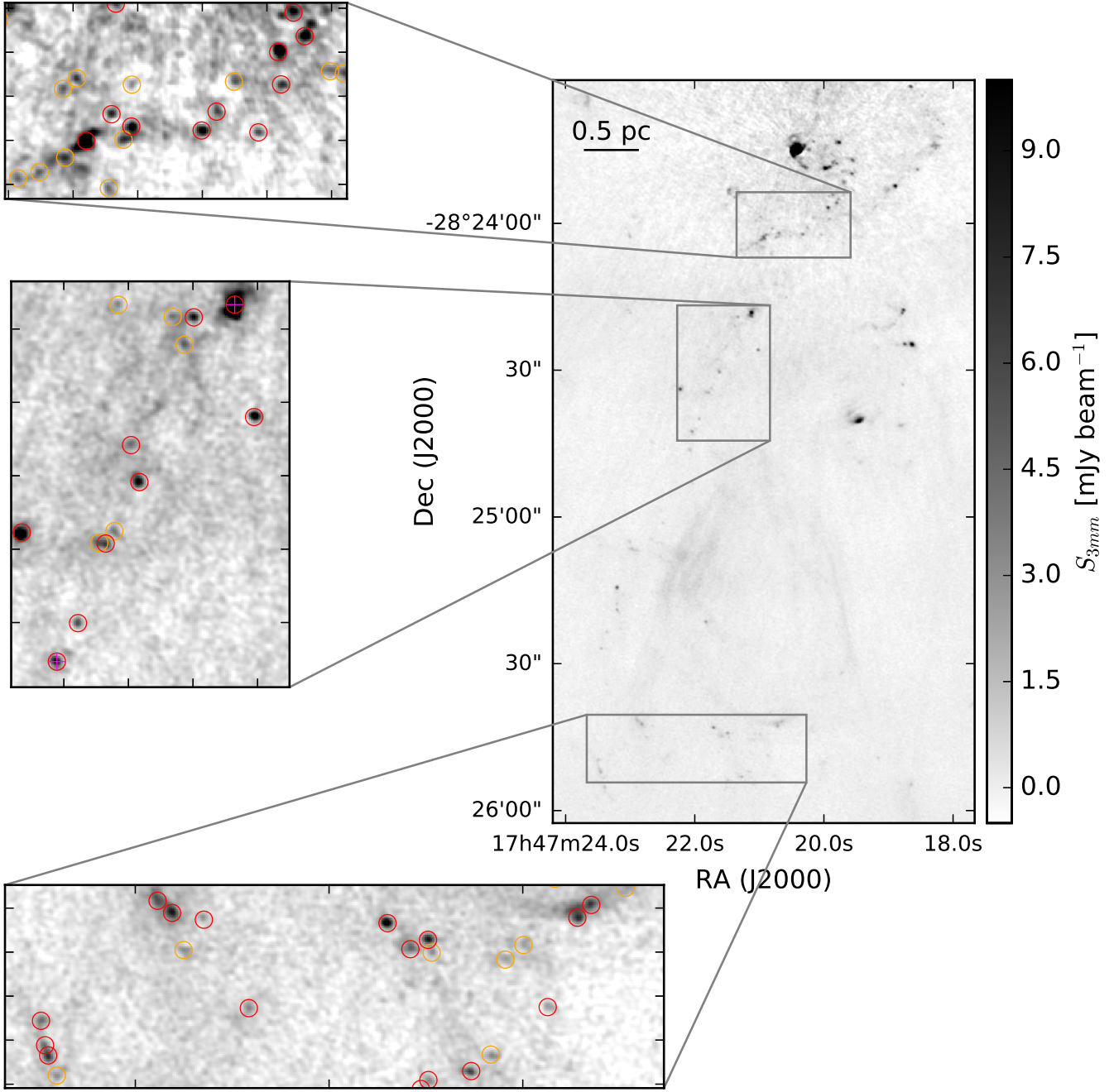


Figure 5. A close-in look at the Sgr B2 DS region. Multiple insets show identified sources in some of the richer sub-regions. The points are colored as in Figure 2. The background image is the ALMA 3 mm continuum.

ternally ionized, mostly neutral gas clumps embedded within diffuse H II regions. They would then be analogous to the heads of cometary clouds, externally ionized globules (“EGGs” Sahai et al. 2012a), or proplyds (externally ionized protoplanetary disks), and their observed emission would give little clue to their nature because the light source is extrinsic.

The majority of the detected sources have size < 4000 AU, i.e., they are unresolved. By contrast, the free-

floating EGGs (“frEGGs”) so far observed have sizes 10,000–20,000 AU (Sahai et al. 2012a,b), so they would be resolved in our observations. Toward the brightest frEGG in Cygnus X, Sahai et al. (2012b) measured a peak intensity $S_{8.5GHz} \approx 1.5$ mJy/beam in a $\approx 3''$ beam. Cygnus X is 6× closer than the Galactic center, so their beam size is the same physical scale as ours. If the free-free emission is thin ($\alpha = -0.1$), the brightness in our data would be $S_{95GHz} = (95/8.5)^{-0.1} S_{8.5GHz} =$

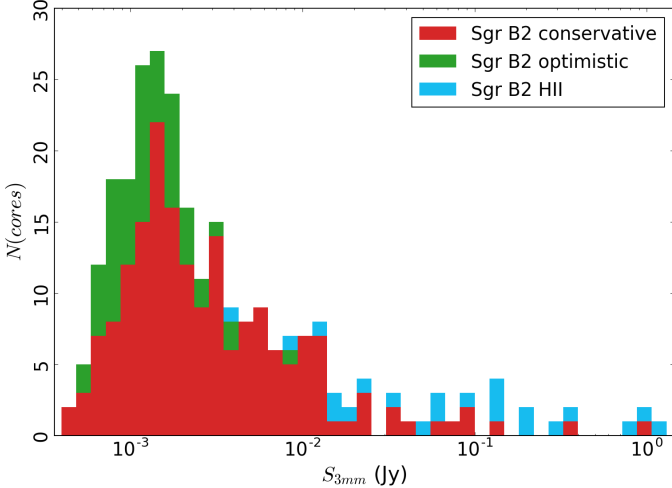


Figure 6. A histogram of the flux density (the peak intensity converted to flux density assuming the source is unresolved) of the observed sources. The histograms are stacked such that there are a total of 27 sources in the highest bin.

$0.79S_{8.5GHz} \approx 1.2$ mJy/beam. These frEGGs would be detectable in our data. Comparison to radio observations at a comparable resolution will be needed to rule out the externally ionized globule hypothesis for the resolved regions within our sample, but the unresolved sources are unlikely to be frEGGs.

If the detected sources were either EGGs or cometary clouds, we would expect them to be located within diffuse H II regions. Many of the sources are near H II regions, as seen in Figure 8a. However, they are nearly all associated with a ridge of HC₃N emission (Figure 8b). If they are deeply embedded within the molecular material, they cannot be externally ionized. The fact that the ionized gas is brightest nearby, rather than directly on top of, the HC₃N suggests that the HC₃N traces a full molecular cloud rather than a thin PDR-like layer, which would be required if these sources are cometary clouds. The association with dense molecular gas implies that the sources are not externally ionized objects.

A final point against the externally ionized hypothesis is the observed spectral indices shown in Figure 7. We measured spectral indices for 60 sources, of which 33 have $\alpha > 2$. These sources are inconsistent with free-free emission and are at least reasonably consistent with dust emission.

3.2.2. Alternative 2: The sources are H II regions produced by interloper ionizing stars

If there is a large population of older (age 1-30 Myr) massive stars, they could ignite compact H II regions when they fly through molecular material. See 3.2.3 for calculations of stationary H II region properties. The

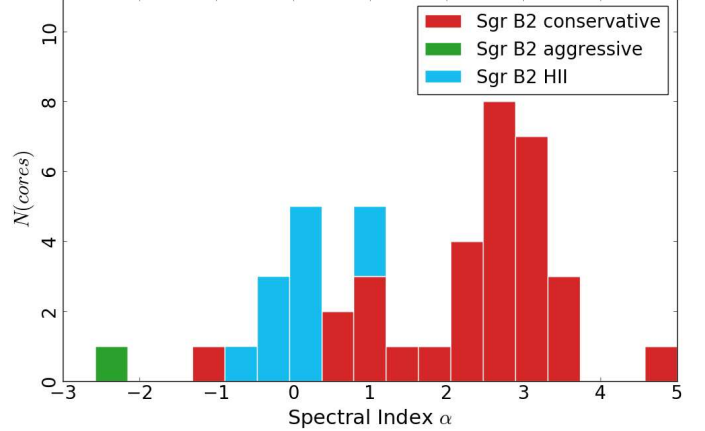


Figure 7. A histogram of the spectral index α for those sources with a statistically significant measurement. The H II regions cluster around $\alpha = 0$, as expected for optically thin free-free emission, while the unclassified sources cluster around $\alpha = 3$, which is weakly consistent with dust emission. There are two particularly notable outliers: the source with a highly negative spectral index, Source 167, has a statistically significant measurement but is in a region of particularly high extended and diffuse background, so the measurement may not be reliable. The other unidentified source with $\alpha \sim -1$ is Source 80, which is very close to the H II region Sgr B2 S, but is not detected in the De Pree et al. (1996) 1.3 cm data; it may be an H II region or it may be contaminated by the nearby H II region.

main problem with this scenario is the spatial distribution of the observed sources. While most of the continuum sources are associated with dense gas and dust ridges, not all of the high-column molecular gas regions have such sources in them (i.e., the left and right sides of the image in Figure 8b, where molecular material is seen with no associated millimeter sources). If there is a free-floating population of OB stars responsible for the 3 mm compact source population, if we assume the spatial distribution of the stars is uniform, the distribution of H II regions surrounding them should match that of the gas (since we are assuming the gas and stars are moving independently). Also, there is no such population of sources seen outside of the dense gas in the infrared (TODO: Who has done infrared studies of Sgr B2? You can infer what I have stated ‘by inspection’ of 2MASS, but it would be more straightforward to quote someone else), which again we should expect if there is a uniformly distributed population. Finally, the spectral indices discussed above (Figure 7) suggest the previously-unidentified sources are dust emission sources, not free-free sources.

3.2.3. Alternative 3: The sources are H II regions produced by recently-formed OB stars

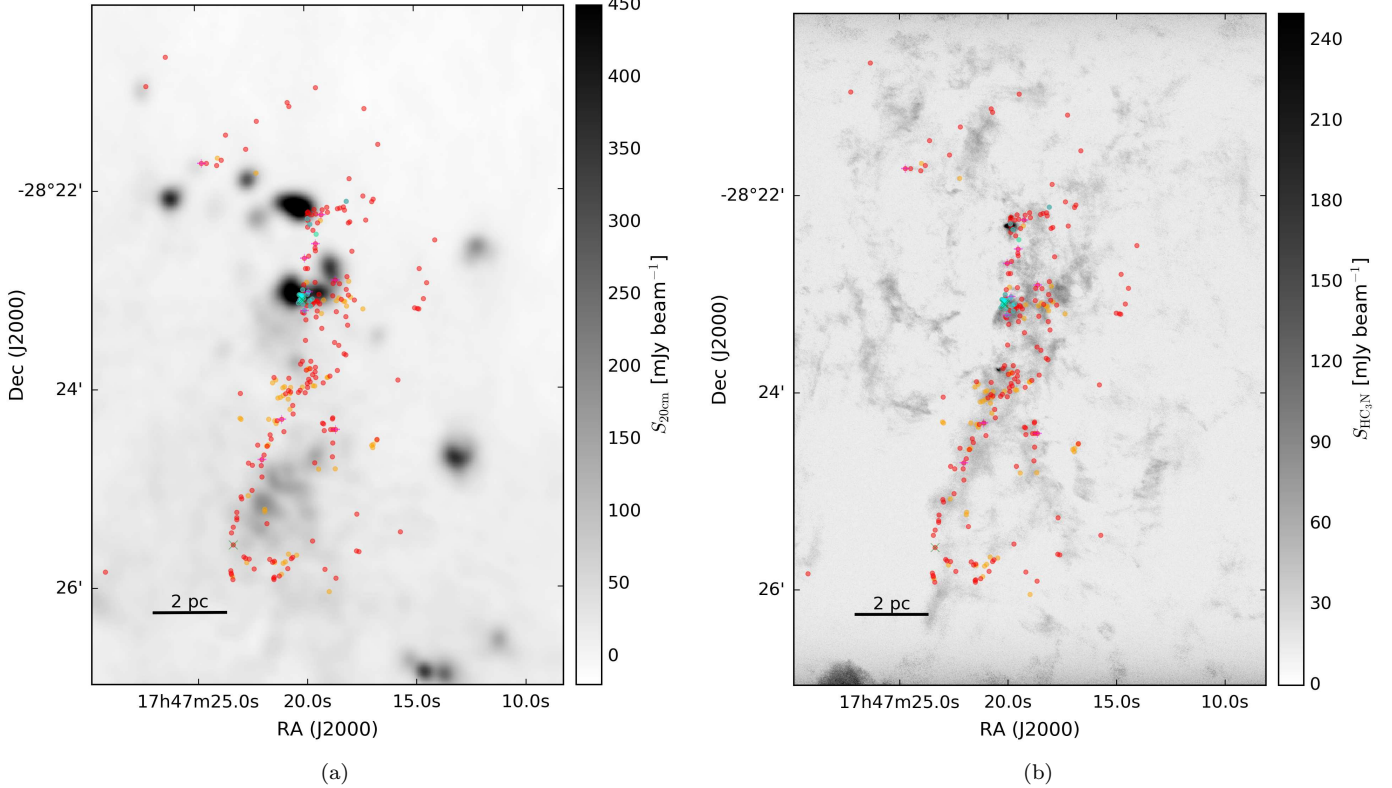


Figure 8. (left) The location of the detected continuum sources (red points) overlaid on a 20 cm continuum VLA map highlighting the diffuse free-free (or possibly synchrotron) emission in the region (Yusef-Zadeh et al. 2004). (right) Continuum sources overlaid on a map of the HC₃N J=10-9 peak intensity over the range [-200, 200] km s⁻¹. HC₃N traces moderate-density molecular gas. In both figures, red dots are ‘conservative’, high-confidence sources, orange dots are ‘optimistic’, low-confidence sources, cyan are H II regions, magenta +’s are masers, and green X’s are X-ray sources.

We know from previous observations (e.g. Mehringer et al. 1995; De Pree et al. 1996, 2015) that there is a substantial population of H II regions in the Sgr B2 clusters. The 23 sources associated with these previously-identified H II regions are among the brightest in our catalog. We address here whether the remaining primarily fainter sources could also be H II regions.

For an unresolved spherically symmetric H II region ($R = 4000$ AU), the expected flux density is $S_{95\text{GHz}} = 4.7$ mJy for a $Q_{lyc} = 10^{47}$ s⁻¹ source (assuming $T_e = 7000$ K), and that value scales linearly with Q_{lyc} as long as the source is optically thin. We rearrange Condon & Ransom (2007) equations 4.60 and 4.61:

$$\begin{aligned}
 S_\nu(Q_{lyc}) &= 4.67 [1 - \exp(c_* T_* \nu_* EM_*)] \\
 \nu_* &= \left(\frac{\nu}{\text{GHz}}\right)^{-2.1} \\
 T_* &= \left(\frac{T_e}{10^4 \text{K}}\right)^{-1.35} \\
 c_* &= -3.28 \times 10^{-7} \\
 EM_* &= \frac{3Q_{lyc}}{4\pi R^2 \alpha_b}
 \end{aligned} \tag{1}$$

where $\alpha_b = 2 \times 10^{-13}$ cm³ s⁻¹, Q_{lyc} is the count rate of ionizing photons in s⁻¹, and R is the H II region radius. The constant c_* was computed by Mezger & Henderson (1967) and is never incorrect by more than $\approx 25\%$.

An extremely compact H II region, e.g., one with $R < 100$ AU and corresponding density $n > 10^6$ cm⁻³, would be optically thick and therefore fainter, $S_{95\text{GHz}}(R = 100\text{AU}, Q_{lyc} = 10^{47}\text{s}^{-1}) = 3.4$ mJy. Even the most luminous O-stars could produce H II regions as faint as 0.5 mJy if embedded in extremely high density gas; above $Q_{lyc} > 10^{47}$ s⁻¹, a 25 AU H II region would be ~ 0.5 mJy.

Figure 9 shows the predicted brightness for various H II regions produced by OB stars and the density required for those H II regions to be the specified size. In order for the detected sources to be O-star-driven H II regions, with $10^{47} < Q_{lyc} < 10^{50}$ s⁻¹, they must be optically thick and therefore extremely compact and dense. There is a narrow range of late O/early B stars, $10^{46} < Q_{lyc} < 10^{47}$ s⁻¹, that could be embedded in compact H II regions of almost any size and produce the observed range of flux densities. Anything fainter, later than \sim B0 ($Q_{lyc} < 10^{46}$ s⁻¹), would be incapable of pro-

ducing the observed flux densities. Any brighter stars would have to be embedded in dust that, at 40 K, would outshine the H II region; more likely, such sources would have much hotter dust and therefore would be much brighter (and more extended) than our observations allow.

The luminosity function of the observed sources is apparently steep, assuming the flux density distribution (Figure 6) represents the luminosity distribution. The observed distribution cuts off near our sensitivity limit, which implies that the steep spectrum should continue to lower luminosities, and therefore there are many more sources below our detection threshold than above. This argument is pure extrapolation, and therefore could easily be wrong, but if there is a large population of sources below $< 0.5 \text{ mJy}$, they are too faint to be H II regions.

This restrictive parameter space, combined with a steep luminosity function, is evidence against the population being dominated by H II regions. The spectral indices also support this conclusion, since some are steeper than $\alpha > 2$ and are therefore inconsistent with free-free emission.

3.2.4. Our hypothesis: The sources are (mostly) protostellar

After ruling out the other possibilities, we test and validate the hypothesis that most or all of the sources are protostellar in this section.

As noted at the top of this section, a cold ‘ prestellar core’ at our detection limit would have $M(20\text{K}) \approx 20 M_{\odot}$. At these high densities ($n \gtrsim 10^8 \text{ cm}^{-3}$), it is unlikely any such cores are unbound. If we assume higher dust temperatures, the inferred gas mass is lower, but an internal heating source - i.e., a protostar - is required. The high density required for our sources results in a very short free-fall timescale, $t_{ff} \lesssim 6000 \text{ yr}$, which suggests that the cores are unlikely to be prestellar cores and instead, even if their emission is dust-dominated, they contain protostars. Their emission is likely dust-dominated, but is probably warmer than the cloud average $\sim 20 - 40 \text{ K}$ (Ginsburg et al. 2016, e.g.).

We cross-matched our source catalog with catalogs of H II regions, X-ray sources, and methanol masers. Associations with these types of sources can be used to classify the sources.

Several sources (23) in our catalog match known H II regions from Gaume et al. (1995) to within $0.5''$, most of which are associated with the brightest sources in our sample; these all have $S_{3\text{mm}} > 9 \text{ mJy}$. The Gaume et al. (1995) catalog does not cover the full observed area, so the H II region source association is incomplete. These sources evidently contain high-mass young stars, but they are not ‘protostars’.

Class II methanol masers are exclusively associated with sites of high-mass star formation. The Caswell et al. (2010) Methanol Multibeam (MMB) Survey identified 11 sources in our observed field of view (their survey covers our entire observed area), of which 10 have a clear match to within $1''$ of a source in our catalog (the MMB catalog sources have a positional accuracy of $\approx 0.4''$, but masers may have an extent up to $1''$). These sources are clearly identified as high-mass protostars.

Some young stars exhibit X-ray emission, including some MYSOs (e.g. Townsley et al. 2014), so we searched for X-ray emission from our sources. 3 of the sources have X-ray counterparts in the Muno et al. (2009) Chandra point source catalog within $1''$. The Muno et al. (2009) catalog covers our entire observed area. The X-ray associated sources most likely either contain protostars or young stars.

We compare our detected sample to that of the Herschel Orion Protostar Survey (HOPS; Furlan et al. 2016) in order to get a general sense of what types of sources we have detected. We selected this survey for comparison because it is one of the largest protostellar core samples with well-characterized bolometric luminosities available. Figure 10 shows the HOPS source flux densities at $870\mu\text{m}$ (from LABOCA on the APEX telescope) scaled to 3 mm assuming a dust opacity index $\beta = 1.5$, which is shallower than usually inferred, so the extrapolated fluxes may be slightly overestimated². The $870\mu\text{m}$ data were acquired with a $\sim 20''$ FWHM beam, which translates to a resolution $\sim 1''$ at $d_{SgrB2} = 8.4 \text{ kpc}$ assuming $d_{Orion} = 415 \text{ pc}$, so our beam size is somewhat smaller than theirs. The HOPS sources are all fainter than the Sgr B2 sources. The brightest HOPS source, with $L_{tot} < 2000 L_{\odot}$, would only be 0.2 mJy in Sgr B2, or about a 4σ source - below our detection threshold even in the noise-free regions of the map. We conclude that the Sgr B2 sources are much more luminous and are therefore massive protostars.

This conclusion is supported by a more direct comparison with the Orion nebula as observed at 3 mm with MUSTANG (Dicker et al. 2009, Figure 11). Their data were taken at $9''$ FWHM resolution, corresponding to $0.48''$ at d_{SgrB2} . The peak flux density measured in that map is toward Source I, $S_{90GHz}(d_{SgrB2}) = 3.6 \text{ mJy}$. Source I would therefore be detected and would be somewhere in the middle of our sample. It is extended, and the extended component would be readily

²We err on the shallower side, implying that the extrapolated 3 mm fluxes are brighter, since this approach gives a more conservative view of the detectability of the Orion sources. In reality, such sources are likely even fainter than predicted here.

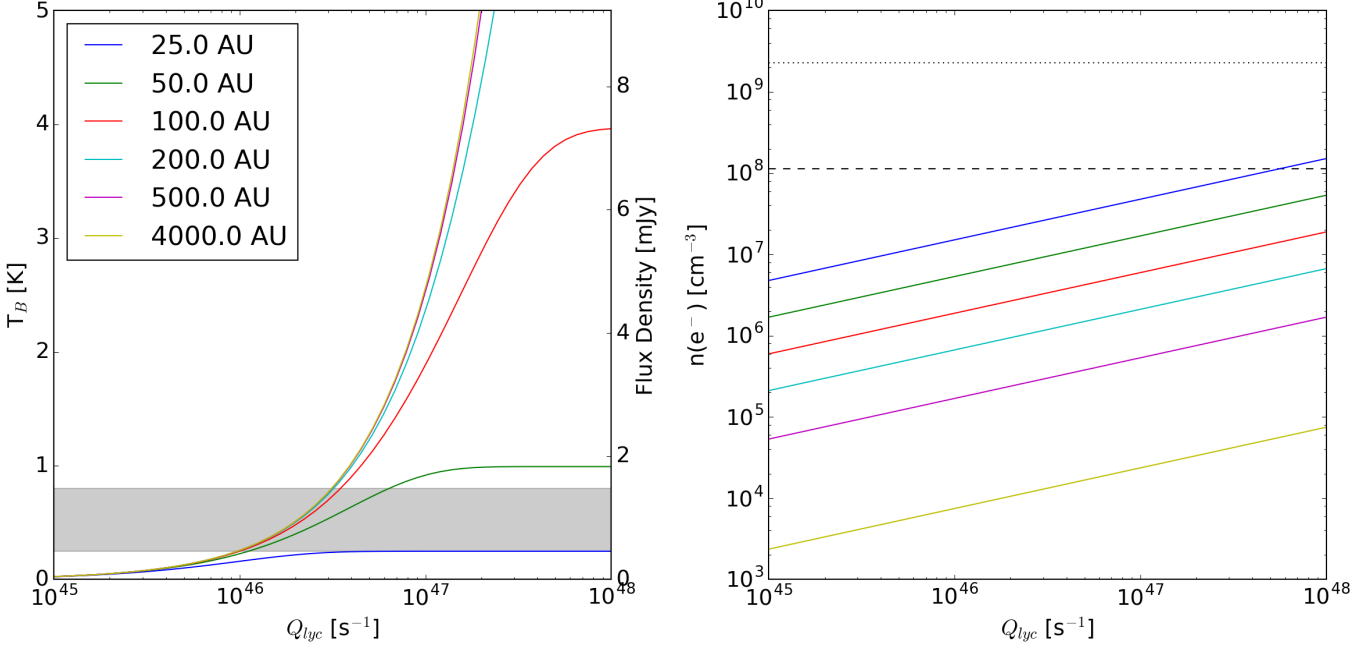


Figure 9. Simple models of spherical H II regions to illustrate the observable properties of such regions. The H II region size is shown by line color; the legend in the left plot applies to both figures. (left) The expected brightness temperature (left axis) and corresponding flux density at 95 GHz within a FWHM=0.5'' beam (right axis) as a function of the Lyman continuum luminosity for a variety of source radii. The grey filled region shows the range of our 5-sigma sensitivity limits, which vary with location from 0.25 to 0.8 K. (right) The density required to produce an H II region of that radius. The horizontal dashed line shows the density corresponding to an unresolved dust source ($r < 0.2'' = 1700$ AU) at the 5- σ detection limit (≈ 0.5 mJy, or about $10 M_\odot$ of dust, assuming $T = 40$ K). Above this line, dust emission would dominate over free-free emission. The dotted line shows the density required for dust emission to produce a 10 mJy source at $T = 40$ K. The density has been scaled by a factor of two, assuming $n_e = 2n(\text{H}_2)$. As seen in the left plot, for any moderate-sized H II region, $R > 100$ AU, a high-luminosity star ($Q_{lyc} > 10^{47} \text{ s}^{-1}$) would produce an H II region brighter than the majority of our sample, which includes only a few sources brighter than 10 mJy. The electron densities required to produce H II regions within our observed range ($1 < S_\nu < 10$ mJy) are fairly extreme, $n_e \gtrsim 10^6 \text{ cm}^{-3}$, for O-stars.

detected in our data. Since Source I is the only known high-mass YSO in the Orion cloud, and it would be detectable while no other sources in the Orion cloud would be, it appears safe to conclude that most of our detected sources are MYSOs.

While we have concluded that the sources are dusty, massive protostars, the spectral indices we measured are somewhat surprising. Typical dust clouds in the Galactic disk have dust opacity indices $\beta \sim 1.5 - 2$ (Schnee et al. 2010; Shirley et al. 2011; Sadavoy et al. 2016). Our spectral indices are lower than these, with only 3 sources having measured $\beta = \alpha - 2 > 1.5$ (at the 2σ level, up to 11 sources are consistent with $\beta = 1.5$, but this is primarily because of their high measurement error). A shallower β implies free-free contamination, large dust grains, or optically thick surfaces are present within our sources. Since the above arguments suggest that the sources are high-mass protostars, the free-free contamination and optically thick inner region models are both plausible.

3.3. Source distribution functions and the star formation rate

In this section we examine the distribution of observed flux densities and the implied total stellar masses.

If we make the very simplistic assumptions that the sources we detect all contain protostars with $L_{bol} \gtrsim 2000 L_\odot$ ($M \gtrsim 8M_\odot$), we can infer the total (proto)stellar mass in the observed region. We assume the stellar masses based on the arguments in Section 3.2.4: in order to be detected, the sources must either be active OB stars illuminating H II regions or cores, or they must be very compact cores with $M > 10 M_\odot$ of warm dust within $R < 4000$ AU. Note that the mass estimates in this section are for the *stars*, not their envelopes.

Using a Kroupa (2001) mass function with $M_{max} = 200 M_\odot$, 23% of the mass is contained in $M > 8M_\odot$ stars. Using the lower-limit mass of $M = 8M_\odot$ as the mass of each of our 263 identified sources, we obtain a total mass $M(> 8) = 2100 M_\odot$. The total stellar mass implied is $M_{tot} = 9 \times 10^3 M_\odot$. If instead we assume

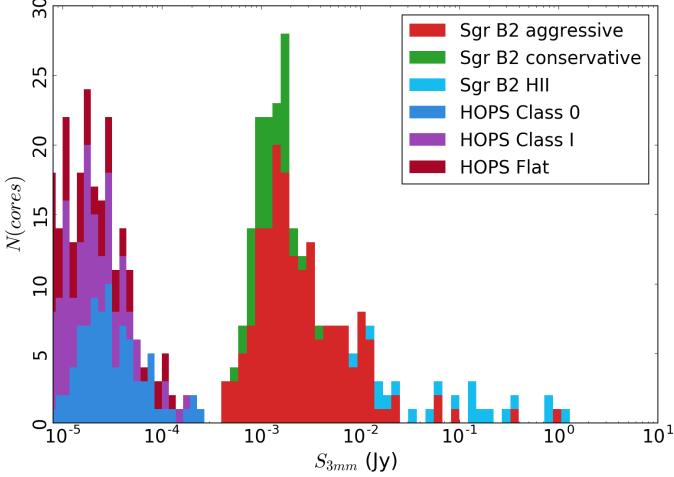


Figure 10. A histogram combining the detected Sgr B2 cores with predicted flux densities based on the HOPS (Furlan et al. 2016) survey. The sources are labeled by their infrared (2-20 μm) spectral index: Class 0 and I have positive spectral index and flat spectrum sources have $-0.3 < \alpha_{IR} < 0.3$. The HOPS histogram shows the 870 μm data from that survey scaled to 3 mm assuming $\beta = 1.5$. Every HOPS source is well below the detection threshold for our observations.

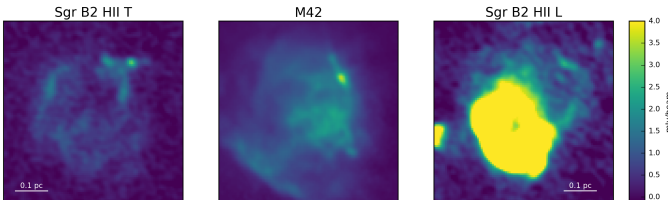


Figure 11. Comparison of two extended HII regions in Sgr B2 to the M42 nebula in Orion. The three panels are shown on the same physical and color scale assuming $d_{Orion} = 415$ pc and $d_{SgrB2} = 8.4$ kpc and that the ALMA and MUSTANG data have the same continuum bandpass. Sgr B2 HII T is comparable in brightness and extent to M42; Sgr B2 HII L is much brighter and is saturated on the displayed brightness scale. The compact source to the top right of the M42 image is Orion Source I; the images demonstrate that Source I and the entire M42 nebula would be easily detected in our data.

each source has a mass equal to the mean stellar mass over the IMF for $M > 8 M_\odot$, $\bar{M} = 21.1 M_\odot$, then the total inferred stellar mass is $M_{tot} = 2.5 \times 10^4 M_\odot$. These are lower limits in the Sgr B2 N and M regions because our catalog is incomplete due to confusion and dynamic range limitations. Additionally, we are using a single-star IMF and our resolution is only ~ 4000 AU, so it is likely that we have undercounted by $\gtrsim 2\times$, since high-mass stars have a high multiplicity fraction (Mason et al. 2009).

For each subcluster identified in Schmiedeke et al. (2016, see Figure 1), we count the number of HII regions identified in our survey plus those identified in previous works (De Pree et al. 1996), and we count the number of protostellar cores not associated with HII regions. To estimate the stellar mass, we assume each core contains a star with $\bar{M}(8 - 20) = 12 M_\odot$ and each HII region contains a \geq B0 star with $\bar{M}(> 20) = 45 M_\odot$. In Table 2, this estimate is shown as M_{count} . We also compute the total stellar mass using the mass fractions $f(M > 20) = 0.14$ and $f(8 < M < 20) = 0.09$. The inferred masses computed from HII region counts and from core counts are shown in columns $M_{inferred,HII}$ and $M_{inferred,cores}$ respectively; $M_{inferred}$ is the average of these two estimates. If our assumptions are correct and the mass distribution is governed by a power-law IMF, we expect $M_{inferred,HII} = M_{inferred,cores}$. Except for Sgr B2 M, the core-based and HII-region based estimates agree to within $\sim 25\%$, which is about as good as expected from Poisson noise in the counting statistics.

Sgr B2 M has the largest sample in both counts and has a factor of nine discrepancy. The discrepancy may arise from the combined effects of source confusion at our 0.5'' resolution and the increased noise around the extremely bright central region that makes detection of < 2 mJy sources difficult. The majority of pixels within the cluster region have significant detections at 3 mm, but we do not presently have the capability to distinguish between extended dust emission, free-free emission, or a confusion-limited source population.

We compare our mass estimates to those of Schmiedeke et al. (2016), who inferred stellar masses primarily from HII region counts. The last two columns of Table 2 show the observed and estimated masses based on HII region counts. For Sgr B2 M and N, our results are similar, as expected since our catalogs are similar. For S and NE, we differ by a large factor, primarily because Schmiedeke et al. (2016) assumed that $M_{min,MYSO}$ and M_{max} were the smallest and largest observed masses in the cluster, while we assumed $M_{min,MYSO} = 8 M_\odot$ and $M_{max} = 200 M_\odot$; i.e., we assumed a spatially invariant IMF.

To determine the star formation rate, we need to know the age of the current star forming burst. We can use the dynamical model of Kruijssen et al. (2015) to get an age of the Sgr B2 cloud $t = 0.74$ Myr (Longmore et al. 2013). To infer the star formation rate, we divide the observed mass by this age; the results are shown in Table 2. This rate assumes that star formation was initiated at the cloud's most recent pericenter passage. The total inferred SFR of the Sgr B2 cloud is $0.036 M_\odot$

Table 2. Cluster Masses

Name	$N(\text{cores})$	$N(\text{HII})$	M_{count}	M_{inferred}	$M_{\text{inferred,HII}}$	$M_{\text{inferred,cores}}$	M_{count}^s	M_{inf}^s	SFR
			M_\odot	M_\odot	M_\odot	M_\odot	M_\odot	M_\odot	$M_\odot \text{ kyr}^{-1}$
M	20	51	2600	9700	17000	2700	1295	20700	13
N	12	7	460	2000	2300	1600	150	2400	2.6
NE	4	2	140	600	650	540	52	1200	0.81
S	5	1	110	500	330	680	50	1100	0.68
Total	240	72	6100	28000	24000	33000	1993	33400	38

M_{count} is the mass of directly counted protostars, assuming each millimeter source is $12.0 M_\odot$, or $45.5 M_\odot$ if it is also an H II region. $M_{\text{inferred,cores}}$ and $M_{\text{inferred,HII}}$ are the inferred total stellar masses assuming the counted objects represent fractions of the total mass 0.09 (cores) and 0.14 (H II regions). M_{inferred} is the average of these two. M_{count}^s and M_{inf}^s are the counted and inferred masses reported in Schmiedeke et al. (2016). The star formation rate is computed using M_{inferred} and an age $t = 0.74$ Myr, which is the time of the last pericenter passage in the Krijssen et al. (2015) model. The *total* column represents the total over the whole observed region. The clusters sum to much less than the *total* because the Deep South region is not included, and it dominates the overall core count.

yr⁻¹, between one quarter and one half of the total for the CMZ (Longmore et al. 2013; Barnes et al. 2017).

3.4. An examination of star formation thresholds

Several authors (e.g., Lada et al. 2010; Heiderman et al. 2010) have proposed that star formation can only occur above a certain density or column density threshold³. We discuss our measurements of column density thresholds in this Section.

3.4.1. Comparison to Lada, Lombardi, and Alves 2010

In this section, we compare the star formation threshold in Sgr B2 to that in local clouds performed by Lada et al. (2010). They determined that all star formation in local clouds occurs above a column density threshold $M_{\text{thresh}} > 116 M_\odot \text{ pc}^{-2}$, or $N_{\text{thresh}}(\text{H}_2) > 5.2 \times 10^{21} \text{ cm}^{-2}$ assuming the mean particle mass is 2.8 amu (Kauffmann et al. 2008). We first note, then, that *all pixels* in our column density maps (Section 2.2, Battersby et al, in prep) are above this threshold by *at least* a factor of 10.

However, Sgr B2 is 8.4 kpc away from us in the direction of our Galaxy’s center, meaning there is a potentially enormous amount of material unassociated with the Sgr B2 cloud along the line of sight. This material may have column densities as low as $5 \times 10^{21} \text{ cm}^{-2}$ or as high as $5 \times 10^{22} \text{ cm}^{-2}$, as measured from relatively blank regions in the Herschel column density map (Battersby et al. 2011). The former value corresponds to the background at high latitudes, $b \sim 0.5$, while the latter is approximately the lowest seen within our field of

³Column density is more commonly used because of its observational convenience, but it is physically meaningless unless high column density leads to high optical depths and thereby changes the gas’s ability to cool.

view. Even with the very aggressive foreground value of $5 \times 10^{22} \text{ cm}^{-2}$ subtracted, nearly the whole Sgr B2 cloud exists above the Lada et al. (2010) threshold.

To directly compare our observations to the star formation thresholds reported in Lada et al. (2010), we examined the column density associated with each millimeter continuum source. The Lada et al. (2010) data used a variable resolution for the column density measurements toward their sample, ranging from 0.06-0.35 pc (equivalent to 1.5 to 9.2'' at a distance of 8.4 kpc). The Herschel data we have available with per-pixel SED fits lack the resolution needed to make a direct comparison to the Lada et al data set, but the SHARC and SCUBA data have resolution approximately equivalent to that used in the Orion molecular cloud in their survey. We therefore use a range of temperatures bracketing the observed range in the Herschel maps ($\sim 20 - 50$ K) to produce column density maps from the SCUBA and SHARC data. Figure 12 shows the cumulative distribution function of the column density associated with each identified continuum source; the column density used is the nearest-neighbor pixel to the source in the column density maps. Even using the conservative maximum temperature $T_{\text{dust}} = 50$ K (resulting in the minimum column density), all of the sources exist at a column density an order of magnitude higher than the Lada threshold, and they exist above that threshold even if the foreground is assumed to be an extreme $5 \times 10^{22} \text{ cm}^{-2}$.

The Lada et al. (2010) sample used Spitzer observations of nearby clouds that were nearly complete to stars at least as small as $0.5 M_\odot$. By contrast, as discussed in Section 3.2.4, our survey is sensitive only to stars with $M \gtrsim 8 M_\odot$. The apparently higher column threshold either means that there is a genuinely higher threshold for star formation in the CMZ or that there is a higher

threshold for high-mass star formation that may still be universal.

Can this discussion be expanded by examining other thresholds? Diederik suggested Krumholz HMF threshold, Kauffmann and Pillai threshold should be examined.

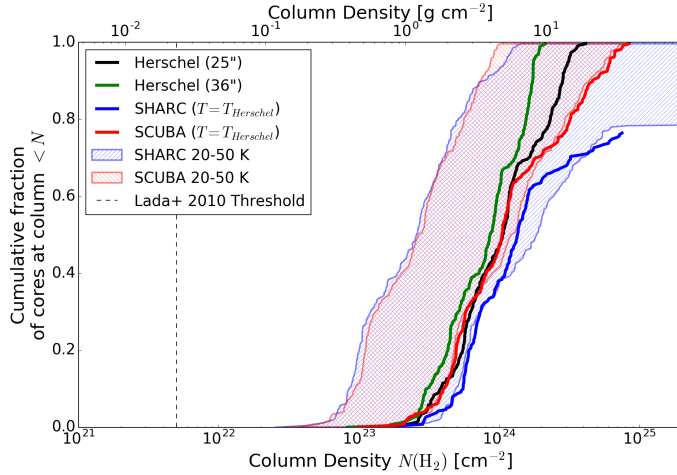


Figure 12. Cumulative distribution functions of the background column density associated with each identified 3 mm continuum source. The column densities are computed from a variety of maps with different resolution and assumed temperature. The Herschel maps use SED-fitted temperatures (Battersby et al. 2017) at 25'' resolution (excluding the 500 μm data point) and 36'' resolution. The SHARC 350 μm and SCUBA 450 μm maps both have higher resolution ($\sim 10''$) but no temperature information; we used an assumed $T_{\text{dust}} = 20$ and $T_{\text{dust}} = 50$ K to illustrate the range of possible background column densities (hatched red and blue). The thick solid red and blue lines show the SHARC and SCUBA column density images using Herschel temperatures interpolated onto their grids: these curves are closer to the 20 K than the 50 K curve and serve as the best estimate column density maps. The SHARC data fail to go to a cumulative fraction of 1 because the central pixels around Sgr B2 M and N are saturated (the lower temperature assumptions result in optical depths > 1 , which cannot be converted to column densities using the optically thin assumption). The vertical dashed line shows the $N(\text{H}_2) = 5.2 \times 10^{21}$ column density threshold from Lada et al. (2010).

3.4.2. Comparison to G0.253+0.016

In G0.253+0.016 (The Brick, G0.253), very little star formation has been observed (Longmore et al. 2013; Johnston et al. 2014; Rathborne et al. 2014, 2015) despite most of the cloud existing above the locally measured Lada et al. (2010) column density threshold. The column density distribution function for G0.253 is shown in Figure 13.

The Rathborne et al. (2014) and Rathborne et al. (2015) data are the deepest observations of G0.253 so far, with a sensitivity about 4× better than ours, but a beam of 1.7'' (similar to that shown in Figure 1; compare to Figure 2 in both Rathborne et al papers). Despite the higher sensitivity of their data, they detected only 3 compact continuum sources. Similarly, Kauffmann et al. (2013) detected no compact continuum sources in their SMA and CARMA observations. By contrast, even in our coarse resolution data, which have a worse sensitivity ($\text{RMS} \approx 0.25 \text{ mJy beam}^{-1}$, 10× worse than Rathborne et al), dozens of compact sources are evident. Our better resolution was critical for identifying the hundreds of sources we have identified, but it is nonetheless evident that the star formation activity is much higher in Sgr B2 than G0.253.

Comparing Sgr B2 to G0.253, the majority of the Sgr B2 cloud is at higher column than G0.253. The presence of star formation in Sgr B2 nearly all occurs at a higher column than exists within G0.253 (Figure 13). The dearth of observed cores in G0.253 is therefore seems most easily explained if there is a column density for star formation that is not reached in G0.253. Given that the G0.253 observations were deeper than our own, yet still identified almost no forming stars, it appears more likely that there is a lack of star formation rather than simply a lack of high-mass star formation. Nonetheless, robust verification of this hypothesis will require much deeper observations.

4. DISCUSSION

We have reported the detection of a large number of point sources and inferred that they are most likely all high-mass protostars. These sources universally reside in gas above $N \gtrsim 2 \times 10^{23} \text{ cm}^{-2}$. In this section, we discuss the implications of this apparent threshold for high-mass star formation in the CMZ.

A theoretical threshold for high-mass star formation, $N > 1 \text{ g cm}^{-2}$ ($N(\text{H}_2) > 2 \times 10^{23} \text{ cm}^{-2}$) was developed by Krumholz & McKee (2008). Nearly all of the sources we have detected reside above this threshold, and we determined our sources are all likely to be massive protostars in Section 3.2.4. However, not all pixels with $N > 1 \text{ g cm}^{-2}$ are forming high-mass stars (Figure 14). We have therefore apparently confirmed that this threshold is a necessary, but not sufficient, condition for high-mass star formation.

4.1. What drives star formation in the greater Sgr B2 complex?

We have shown that, in addition to the known forming massive clusters, star formation is ongoing in an extended and elongated region to the north and south.

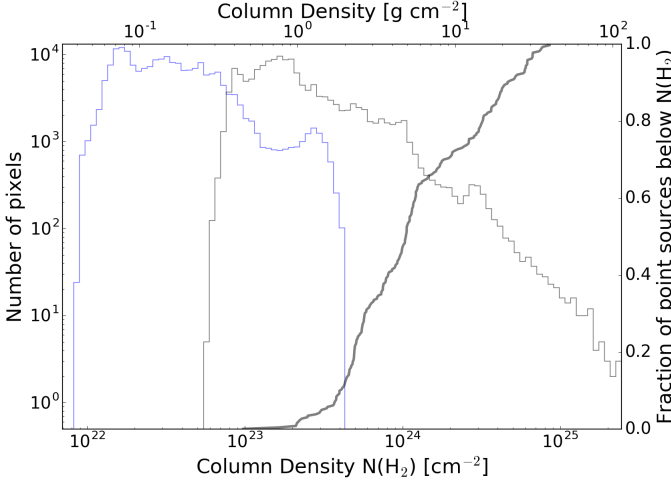


Figure 13. Histograms of the column density of G0.253+0.016 (blue) and Sgr B2 (gray) using the combined SCUBA 450 μm and Herschel 500 μm intensity with the interpolated Herschel dust temperatures. The cumulative distribution of core ‘background’ column densities in Sgr B2 is shown as a thick gray line, showing that the densities at which stars are forming in Sgr B2 are barely reached in G0.253.

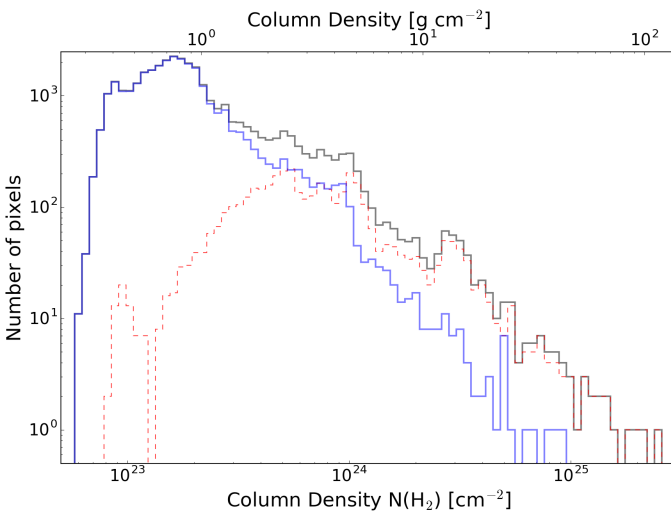


Figure 14. Histograms of the column density measured with the combined SCUBA and Herschel data using the interpolated Herschel temperatures covering only the region observed with ALMA. The black histogram shows the whole observed region, the blue solid shows the SCUBA pixels that do not contain an ALMA source, and the red dashed region shows those pixels that are within one beam FWHM of an ALMA source. While the ALMA sources (high mass protostars and young stars) clearly reside in high-column gas, there is abundant high-column material that shows no signs of ongoing star formation.

Excluding the clusters, most of the newly discovered sources trace out long and linear features. Why are the sources aligned? Was star formation in Sgr B2 triggered by a single event?

There are a few different possible triggers that have been considered in the literature: pericenter passage (Kruisssen et al. 2015), cloud-cloud collision (Hasegawa et al. 1994; Mehringer & Menten 1997; Sato et al. 2000), and expanding shells driven by massive stars (Martín-Pintado et al. 1999). These scenarios are distinct and apply to different scales. The pericenter passage model assumes that gas is fed into a ~ 100 pc radius non-circular orbit and experiences significant tidal compression at closest approach to the bottom of the gravitational potential. The compression leads to progressively increasing star formation along the CMZ dust ridge. Cloud-cloud collision models assume that independent clouds on different orbits are interacting. The expanding shell model assumes the shells are driven by feedback from a previously formed generation of high-mass stars.

We examine these three possibilities but reach no definitive conclusion about which process is dominant.

4.1.1. Pericenter Triggering

Our observations are reconcilable with a star formation event triggered at pericenter passage. If the entire cloud was stable prior to pericenter passage, at closest approach it would have been simultaneously crushed and stretched by shear (Kruisssen et al. 2015). This event would have driven collapse of the whole cloud, with the densest regions collapsing fastest and possibly forming the clusters we observe today. This model is discussed further in Section 4.2.

4.1.2. Cloud-cloud collision

There are no definitive signs of ‘cloud-cloud collision’ or ‘colliding flows’ in our line or continuum data, though that is largely because all possible evidence for such flows is highly ambiguous. For example, Haworth et al. (2015) show some of the best cases for cloud-cloud collision using the ‘extended bridge’ in position-velocity between two colliding clouds, but these signatures can be completely hidden when multiple clouds exist along a line of sight, as in Sgr B2. We cannot rule out cloud-cloud collision, but neither can we provide evidence to support it.

Most of the notable kinematic features evident in the dense gas images can be attributed to expanding H II regions or otherwise feedback-driven flows (see Section 4.1.3). While interacting independent gas streams are a possible agent affecting Sgr B2, their effects are not obvious in our core catalog or in the gas data cubes.

We note that some ‘colliding flows’ are expected in almost any collapse scenario. For example, simulations of a cloud passing through Galactic pericenter (Kruijssen et al. in prep.; Dale et al. in prep.) show that some material is ejected during this passage that later collapses back onto the original cloud. It is possible that any apparent colliding flows (e.g. Sato et al. 2000) are a relic of this process.

4.1.3. Expanding Shells

There is evidence of expanding shells in Sgr B2, but these shells are not uniformly sites of star formation. There are four shell examples we consider: Sgr B2 DS, Sgr B2 N/NE, Sgr B2 E, and Sgr B2 W. Two of these (N/NE and DS) show signs of star formation, two (E and W) do not.

There is extended ionized emission in Sgr B2 Deep South that appears to be a bubble surrounded by the millimeter continuum sources. While this region looks like a normal H II region in the 12'' resolution 20 cm VLA data in Figure 8, the 3 mm continuum reveals long filamentary features reminiscent of the Galactic center arched filaments. By analogy, they may be magnetically dominated regions, but there must be some central source of ionizing radiation or energetic particles. Whatever the driver, it is possible that an expanding bubble of hot gas has compressed the molecular material along the ridge where we observe star formation. However, the ridge of millimeter sources extends well above the apparent bubble edge, so it is unlikely that the entire DS ridge was driven by a single coherent expanding bubble.

By contrast, the Sgr B2 North bubble does not contain any ionized emission. It contains fewer total sources, which trace the edge of an expanding bubble previously noted by de Vicente et al. (1997). The coincidence of star forming cores along the edge of a bubble again suggests some sort of compressional triggering.

However, while both N/NE and DS show circumstantial, morphological evidence for a compressional event, there are other regions within our map that show the same general morphology in the gas yet exhibit no star formation. Sgr B2 E and W are the regions east and west of the central ridge, respectively.

Shell-like features in Sgr B2 E can be seen in Figure 15. The molecular gas, as traced by HC₃N in this case, outlines bubble edges to the east of Sgr B2 M: the HC₃N outlines a cavity in the column density map. The edge of this eastern bubble has a lower average column density than either the northern Sgr B2 NE or the Sgr B2 DS regions, and it shows no signs of ongoing star formation.

In Sgr B2 W, there is a secondary ridge of HC₃N emission paralleling the central ridge. No MYSOs are detected in this ridge.

We observe that some sources appear to be associated with shells, but there are some shells that have no associated ongoing star formation. Most of the observed star formation is not along shell edges. We therefore conclude that, while the expanding shells may have some effect on where MYSOs are forming, it appears that these shells do not provide a sufficient condition to drive star forming bursts.

4.2. The clusters and the extended population

We noted in Section 3.3 that the H II-region-inferred protostellar mass matches the core-inferred protostellar mass to within a factor of 2 in the whole Sgr B2 cloud and the individual clusters excepting Sgr B2 M. In Sgr B2 M, the H II-region inferred mass is $\sim 9 \times$ greater than the core-inferred mass. While the lack of faint sources in Sgr B2 M could be an observational limitation, it may be a real effect signifying an evolutionary difference.

Sgr B2 M has more H II regions and is more centrally condensed than any of the other clusters and the distributed star forming population. Assuming that H II regions represent a later stage in protostellar evolution than the dusty protostellar core stage, this difference implies that Sgr B2 M is older than Sgr B2 N and the distributed protostellar population. By contrast, along the Sgr B2 DS ridge, there are no H II regions, but there are ~ 100 high-mass protostars, which implies that these protostars began their formation nearly simultaneously.

The large number of probable protostars observed along an elongated ridge allows us to estimate an upper limit on their age. Assuming all of these forming stars are bound to the cloud and/or central clusters, they should approach a spherical distribution within about one crossing time (Efremov & Elmegreen 1998). If we assume the turbulent velocity dispersion is $\sigma_{1D} \approx 10$ km s⁻¹ (e.g. Henshaw et al. 2016), and the length of the DS ridge is $L \approx 10$ pc, the upper limit on the formation time of the protostars is $L/\sigma_{1D} < 1$ Myr. Given the tight alignment of the protostars with the gas ridge (Figures 8 and 15), it is possible to establish a lower upper limit. Most of the sources are within $r < 0.5$ pc of the ‘ridge’, which suggests an upper age limit $t < r/\sigma_{1D} = 5 \times 10^4$ yr; however, if the sources have a lower velocity dispersion, this limit would be higher. Nonetheless, the DS ridge sources appear to be recently formed.

The expanding H II regions observed around Sgr B2 M and N (and assumed to be associated with them) give a lower limit on their ages. The HII regions I, J, A1, and

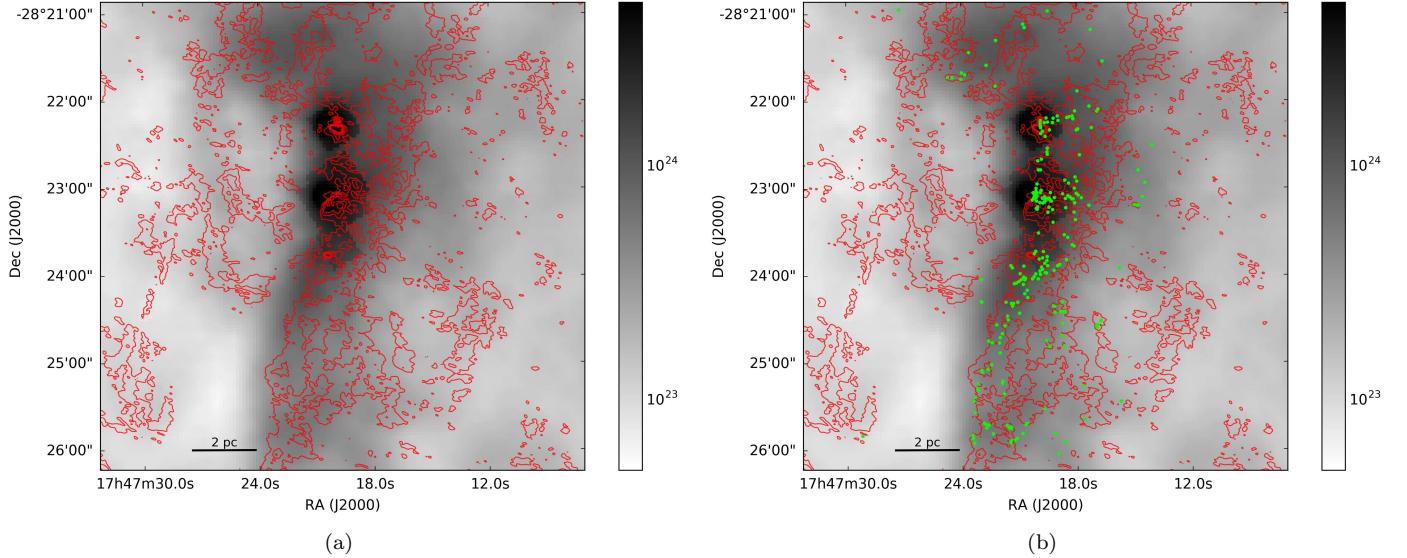


Figure 15. ALMA HC_3N peak intensity contours (red) overlaid on the derived SCUBA column density image using Herschel Hi-Gal interpolated temperatures. The HC_3N was shown in grayscale in Figure 8. Contours are at levels [3,7,11,15,19,23] K. The HC_3N bubble edges can be seen surrounding cavities in the SCUBA column density map on the east side of the main ridge. To the north, the HC_3N also traces bubbles, but these are less evident in this velocity-integrated view. The important feature discussed in Section 4.1 is the differing column density around each of the bubbles. The right figure has the cores overlaid as green dots, showing that the 3 mm sources closely trace the molecular gas, but not all dense molecular gas contains cores or protostars.

K4 have radii $r \approx 0.1$ pc (Gaume et al. 1995), suggesting their ages are at least $t > 10^5$ yr assuming they are expanding into a density $n \gtrsim 10^5 \text{ cm}^{-3}$ (de Pree et al. 1995; Schmiedeke et al. 2016). The clusters therefore appear to be somewhat older than the ridge sources.

The relative ages of M and the rest of the region (i.e., Sgr B2 M is apparently older) suggest two possibilities for their formation history. If we take the ages at face value, Sgr B2 M must have collapsed first to form stars in an early event, then sometime later the DS ridge collapsed to form stars in a later event. A second possibility is that the overall collapse of both Sgr B2 M and DS began at the same time, but the Sgr B2 M region was denser and therefore had a shorter collapse time, which is predicted by hierarchical cluster formation models to lead to higher star formation efficiencies (Kruyssen 2012). Our catalog does not allow us to distinguish these possibilities. However, the latter scenario would predict that the cloud should be in a state of global collapse, with the least dense regions collapsing most slowly. This collapse has been suggested to be ongoing in CMZ clouds by Walker et al. (2015, 2016) and may leave detectable kinematic signatures (e.g., self-absorption in moderately optically thick lines) in the dense gas.

5. CONCLUSIONS

We have reported the detection of 263 3 mm point sources in the extended Sgr B2 cloud and determined that the majority are high-mass protostellar cores. This survey represents the first large population of protostars detected in the Galactic center and represents the largest sample yet reported of high-mass protostars.

The large population of high-mass protostellar cores indicates that the entire Sgr B2 cloud, not just the well-known clusters N, M, and S, is undergoing a burst of star formation. More than half of the currently forming generation of stars is not associated with any of the clusters but is instead part of the extended burst, as is predicted by models of hierarchical star and cluster formation.

Using Herschel, SCUBA, and SHARC data, we have measured a threshold for high-mass star formation analogous to that done in local clouds by Lada et al. (2010). We find that there are no high-mass protostars in gas below $N < 10^{23} \text{ cm}^{-2}$, and half are found above $N > 10^{24} \text{ cm}^{-2}$, at a resolution of $\approx 10'' = 0.4$ pc. It is not yet clear whether there is a higher threshold for low-mass star formation, but the threshold for high-mass star formation appears consistent with that theorized for Galactic plane conditions.

The large detected population of high-mass protostars implies a much larger population of as-yet undetectable lower-mass protostars. Future ALMA and JWST programs to probe this population would provide the data needed to directly compare star formation thresholds in

the most intensely star-forming cloud in our Galaxy to those in nearby clouds.

Software: The software used to make this version of the paper is available from github at https://github.com/keflavich/SgrB2_ALMA_3mm_Mosaic/ with hash 8089c07(2017-06-21).

Acknowledgements This work is partly supported by a grant from the National Science Foundation (AST-1615311, De Pree). JMDK gratefully acknowledges

funding from the German Research Foundation (DFG) in the form of an Emmy Noether Research Group (grant number KR4801/1-1), from the European Research Council (ERC) under the European Union’s Horizon 2020 research and innovation programme via the ERC Starting Grant MUSTANG (grant agreement number 714907), and from Sonderforschungsbereich SFB 881 “The Milky Way System” (subproject P1) of the DFG.

REFERENCES

- Bally, J., Aguirre, J., Battersby, C., et al. 2010, ApJ, 721, 137
- Barnes, A. T., Longmore, S., Battersby, C., Bally, J., & Kruijssen, J. M. D. 2016, arXiv:1609.08478v1
- Barnes, A. T., Longmore, S. N., Battersby, C., et al. 2017, ArXiv e-prints, arXiv:1704.03572
- Battersby, C., Bally, J., & Svoboda, B. 2017, ApJ, 835, 263
- Battersby, C., Bally, J., Ginsburg, A., et al. 2011, A&A, 535, A128
- Bendo, G. J., Griffin, M. J., Bock, J. J., et al. 2013, MNRAS, 433, 3062
- Caswell, J. L., Fuller, G. A., Green, J. A., et al. 2010, MNRAS, 404, 1029
- Chapin, E. L., Berry, D. S., Gibb, A. G., et al. 2013, MNRAS, 430, 2545
- Condon, J. J., & Ransom, S. 2007, Essential Radio Astronomy (NRAO).
<http://www.cv.nrao.edu/course/astr534/ERA.shtml>
- De Pree, C. G., Gaume, R. A., Goss, W. M., & Claussen, M. J. 1996, ApJ, 464, 788
- de Pree, C. G., Rodriguez, L. F., & Goss, W. M. 1995, RMxAA, 31, 39
- De Pree, C. G., Peters, T., Low, M. M. M., et al. 2015, arXiv:1511.05131v1
- de Vicente, P., Martin-Pintado, J., & Wilson, T. L. 1997, A&A, 320, 957
- Di Francesco, J., Johnstone, D., Kirk, H., MacKenzie, T., & Ledwosinska, E. 2008, ApJS, 175, 277
- Dicker, S. R., Mason, B. S., Korngut, P. M., et al. 2009, ApJ, 705, 226
- Dowell, C. D., Lis, D. C., Serabyn, E., et al. 1999, in Astronomical Society of the Pacific Conference Series, Vol. 186, The Central Parsecs of the Galaxy, ed. H. Falcke, A. Cotera, W. J. Duschl, F. Melia, & M. J. Rieke, 453
- Efremov, Y. N., & Elmegreen, B. G. 1998, MNRAS, 299, 588
- Furlan, E., Fischer, W. J., Ali, B., et al. 2016, ApJS, 224, 5
- Gaume, R. A., Claussen, M. J., de Pree, C. G., Goss, W. M., & Mehringer, D. M. 1995, ApJ, 449, 663
- Ginsburg, A., Glenn, J., Rosolowsky, E., et al. 2013, ApJS, 208, 14
- Ginsburg, A., Walsh, A., Henkel, C., et al. 2015, A&A, 584, L7
- Ginsburg, A., Henkel, C., Ao, Y., et al. 2016, A&A, 586, A50
- Hasegawa, T., Sato, F., Whiteoak, J. B., & Miyawaki, R. 1994, ApJL, 429, L77
- Haworth, T. J., Shima, K., Tasker, E. J., et al. 2015, arXiv:1509.00859v1
- Heiderman, A., Evans, II, N. J., Allen, L. E., Huard, T., & Heyer, M. 2010, ApJ, 723, 1019
- Henshaw, J. D., Longmore, S. N., Kruijssen, J. M. D., et al. 2016, MNRAS, 457, 2675
- Higuchi, A. E., Hasegawa, T., Saigo, K., Sanhueza, P., & Chibueze, J. O. 2015, ApJ, 815, 106
- Immer, K., Kauffmann, J., Pillai, T., Ginsburg, A., & Menten, K. M. 2016, A&A, 595, A94
- Johnston, K. G., Beuther, H., Linz, H., et al. 2014, A&A, 568, A56
- Jones, P. A., Burton, M. G., Cunningham, M. R., et al. 2012, MNRAS, 419, 2961
- Kauffmann, J., Bertoldi, F., Bourke, T. L., Evans, II, N. J., & Lee, C. W. 2008, A&A, 487, 993
- Kauffmann, J., Pillai, T., & Zhang, Q. 2013, ApJL, 765, L35
- Kauffmann, J., Pillai, T., Zhang, Q., et al. 2016a, ArXiv e-prints, arXiv:1610.03499
- . 2016b, ArXiv e-prints, arXiv:1610.03502
- Kroupa, P. 2001, MNRAS, 322, 231
- Kruijssen, J. M. D. 2012, MNRAS, 426, 3008
- Kruijssen, J. M. D., Dale, J. E., & Longmore, S. N. 2015, MNRAS, 447, 1059
- Kruijssen, J. M. D., & Longmore, S. N. 2013, MNRAS, 435, 2598
- Krumholz, M. R., & McKee, C. F. 2008, Nature, 451, 1082

- Lada, C. J., Lombardi, M., & Alves, J. F. 2010, *ApJ*, 724, 687
- Longmore, S. N., Kruijssen, J. M. D., Bally, J., et al. 2013, *MNRAS*, 433, L15
- Lu, X., Zhang, Q., Kauffmann, J., et al. 2016, arXiv:1609.08240v1
- Martín-Pintado, J., Gaume, R. A., Rodríguez-Fernández, N., de Vicente, P., & Wilson, T. L. 1999, *ApJ*, 519, 667
- Mason, B. D., Hartkopf, W. I., Gies, D. R., Henry, T. J., & Helsel, J. W. 2009, *AJ*, 137, 3358
- Mehringer, D. M., de Pree, C. G., Gaume, R. A., Goss, W. M., & Claussen, M. J. 1995, *ApJL*, 442, L29
- Mehringer, D. M., & Menten, K. M. 1997, *ApJ*, 474, 346
- Mezger, P. G., & Henderson, A. P. 1967, *ApJ*, 147, 471
- Molinari, S., Swinyard, B., Bally, J., et al. 2010, *A&A*, 518, L100
- Molinari, S., Schisano, E., Elia, D., et al. 2016, *A&A*, 591, A149
- Muno, M. P., Bauer, F. E., Baganoff, F. K., et al. 2009, *ApJS*, 181, 110
- Ossenkopf, V., & Henning, T. 1994, *A&A*, 291, 943
- Ossenkopf-Okada, V., Csengeri, T., Schneider, N., Federrath, C., & Klessen, R. S. 2016, *A&A*, 590, A104
- Pierce-Price, D., Richer, J. S., Greaves, J. S., et al. 2000, *ApJL*, 545, L121
- Rathborne, J. M., Longmore, S. N., Jackson, J. M., et al. 2014, *ApJ*, 786, 140
- . 2015, *ApJ*, 802, 125
- Rau, U., & Cornwell, T. J. 2011, *A&A*, 532, A71
- Reid, M. J., Menten, K. M., Zheng, X. W., Brunthaler, A., & Xu, Y. 2009, *ApJ*, 705, 1548
- Sadavoy, S. I., Stutz, A., Schnee, S., et al. 2016, arXiv:1601.06769v1
- Sahai, R., Güsten, R., & Morris, M. R. 2012a, *ApJL*, 761, L21
- Sahai, R., Morris, M. R., & Claussen, M. J. 2012b, *ApJ*, 751, 69
- Sanchez-Monge, A., Schilke, P., Schmiedeke, A., et al. 2017, ArXiv e-prints, arXiv:1704.01805
- Sato, F., Hasegawa, T., Whiteoak, J. B., & Miyawaki, R. 2000, *ApJ*, 535, 857
- Schmiedeke, A., Schilke, P., Möller, T., et al. 2016, *A&A*, 588, A143
- Schnee, S., Enoch, M., Noriega-Crespo, A., et al. 2010, *ApJ*, 708, 127
- Shetty, R., Beaumont, C. N., Burton, M. G., Kelly, B. C., & Klessen, R. S. 2012, *MNRAS*, 425, 720
- Shirley, Y. L., Mason, B. S., Mangum, J. G., et al. 2011, *AJ*, 141, 39
- Stanimirovic, S. 2002, in *Astronomical Society of the Pacific Conference Series*, Vol. 278, Single-Dish Radio Astronomy: Techniques and Applications, ed. S. Stanimirovic, D. Altschuler, P. Goldsmith, & C. Salter, 375–396
- Townsley, L. K., Broos, P. S., Garmire, G. P., et al. 2014, *ApJS*, 213, 1
- Walker, D. L., Longmore, S. N., Bastian, N., et al. 2016, *MNRAS*, 457, 4536
- . 2015, *MNRAS*, 449, 715
- Wenger, M., Ochsenbein, F., Egret, D., et al. 2000, *A&AS*, 143, 9
- Yusef-Zadeh, F., Hewitt, J. W., & Cotton, W. 2004, *ApJS*, 155, 421

APPENDIX

A. SINGLE DISH COMBINATION

To measure the column density at a resolution similar to Lada et al. (2010), we needed to use ground-based single-dish data with resolution $\sim 10''$. We combined these images with Herschel data, which recover all angular scales, to fill in the missing ‘short spacings’ from the ground-based data.

Specifically, we combine the SHARC 350 μm (Dowell et al. 1999) and SCUBA 450 μm (Pierce-Price et al. 2000; Di Francesco et al. 2008) with Herschel 350 and 500 μm data (Molinari et al. 2016), respectively.

Combining single-dish with ‘interferometer’ data, or data that are otherwise insensitive to large angular scales, is not a trivial process. The standard approach advocated by the ALMA project is to use the ‘feather’ process, in which two images are fourier-transformed, multiplied by a weighting function, added together, and fourier transformed back to image space (see equations in §5.2 of Stanimirovic 2002). This process is subject to substantial uncertainties, particularly in the choice of the weighting function.

Two factors need to be specified for linear combination: the beam size of the ‘single-dish’, or total power, image, and the largest angular scale of the ‘interferometer’ or filtered image. While the beam size is sometimes well-known, for single dishes operating at the top of their usable frequency range (e.g., the CSO at 350 μm or GBT at 3 mm), there are uncertainties in the beam shape and area and there are often substantial sidelobes. In interferometric data, the largest angular scale is well-defined in the originally sampled UV data, but is less well-defined in the final image because different weighting factors change the recovered largest angular scale. For ground-based filtered data, the largest recoverable angular scale is difficult to determine and requires concerted effort (e.g., Ginsburg et al. 2013; Chapin et al. 2013).

To assess the uncertainties in image combination, particularly on the brightness distribution (e.g. Ossenkopf-Okada et al. 2016), we have performed a series of experiments combining the Herschel with the SCUBA data using different weights applied to the SCUBA data. As discussed in Section 2, we empirically determined the scale factor required for the best match between SCUBA and Herschel data was $3\times$, which is shockingly large but justifiable. In the experiment shown in Figure 16, we show the images and resulting histograms when we combine the Herschel data with the SCUBA data scaled by a range of factors from $0.5\times$ to $10\times$. The changes to the high end of the histogram are dramatic, but the middle region containing most of the pixels (and most relevant to the discussion of thresholds in the paper) is hardly affected. Additionally, we show the cumulative distribution function of core background surface brightnesses (as in Figure 12), showing again that only the high end is affected.

B. SELF-CALIBRATION

We demonstrate the impact of self-calibration in this section. The adopted approach used three iterations of phase-only self-calibration followed by two iterations of phase and amplitude self-calibration. Each iteration involved slightly different imaging parameters. The final, deepest clean used a threshold mask on the previous shallower clean. The script used to produce the final images is available at https://github.com/keflavich/SgrB2_ALMA_3mm_Mosaic/blob/8089c07/script_merge/selfcal_continuum_merge_7m.py. The effects are shown with a cutout centered on the most affected region around Sgr B2 M in Figure 17.

C. PHOTOMETRIC CATALOG

We include the full catalog in digital form (https://github.com/keflavich/SgrB2_ALMA_3mm_Mosaic/blob/master/tables/continuum_photometry_withSIMBAD_andclusters.ipac). Table ?? shows the brightest 35 sources; the rest are included in a digital-only catalog. Sources are labeled based on an arbitrary source number plus any pre-existing catalog name. If a source is associated with a cluster, it has an entry corresponding to that cluster in the `Cluster` column; association is determined by checking whether a source is within a particular distance of the cluster center as defined by Schmiedeke et al. (2016). A source `Classification` column is included, which states whether the source is a strong or weak detection, whether it has an X-ray association, whether it has a maser association, and its SIMBAD classification if it has one. Measurements reported include the peak flux density $S_{\nu,max}$, the corresponding brightness temperature $T_{B,max}$, the integrated flux density within a beam ($0.5''$) radius, the background RMS flux level σ_{bg} as an estimate of the local noise, the spectral index α and the error on that $E(\alpha)$. Mass and column density estimates are given for an assumed temperature $T = 40$ K (M_{40K} and $N(\text{H}_2)_{40K}$). For sources with $T_{B,max} \gtrsim 20$ K, these estimates are unlikely to be useful since the assumed temperature is probably lower than the true temperature.

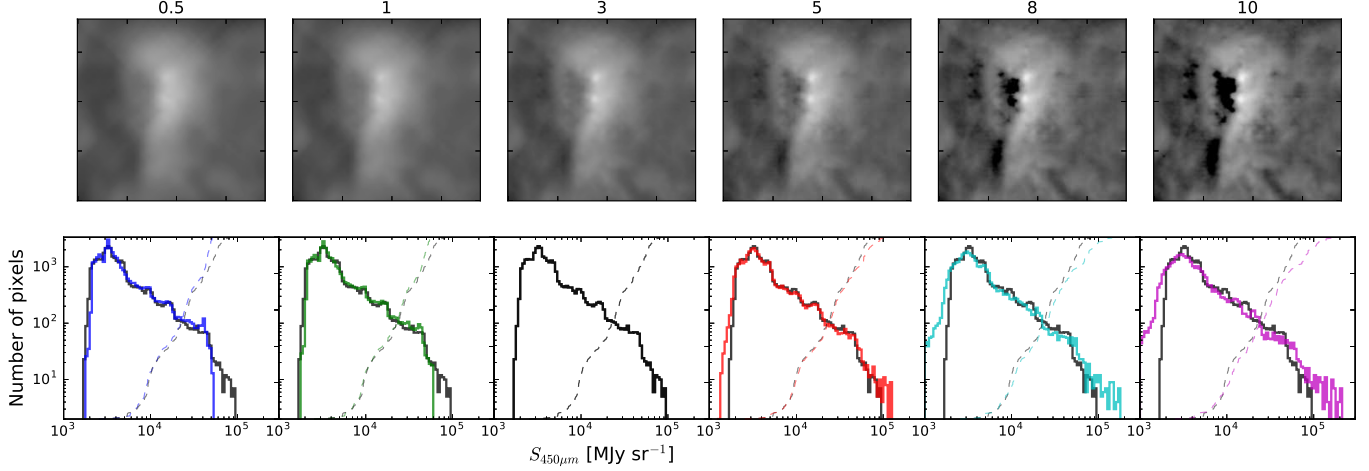


Figure 16. A demonstration of the effects of using different calibration factors when combining the SCUBA data with the Herschel data using the ‘feather’ process. The numbers above each panel show the scale factor applied to the SCUBA data before fourier-combining it with the Herschel data. The factor of 3 was used in this paper and shows the most reasonable balance between the high-resolution of the SCUBA data and the all-positive Herschel data. In the lower panels, the fiducial scale factor of 3 is shown in black in all panels. The solid lines show histograms of the images displayed in the top panels. The dashed lines show the cumulative distribution of the background surface brightnesses of the point sources in this sample; they are similar to the distributions shown in Figure 12.

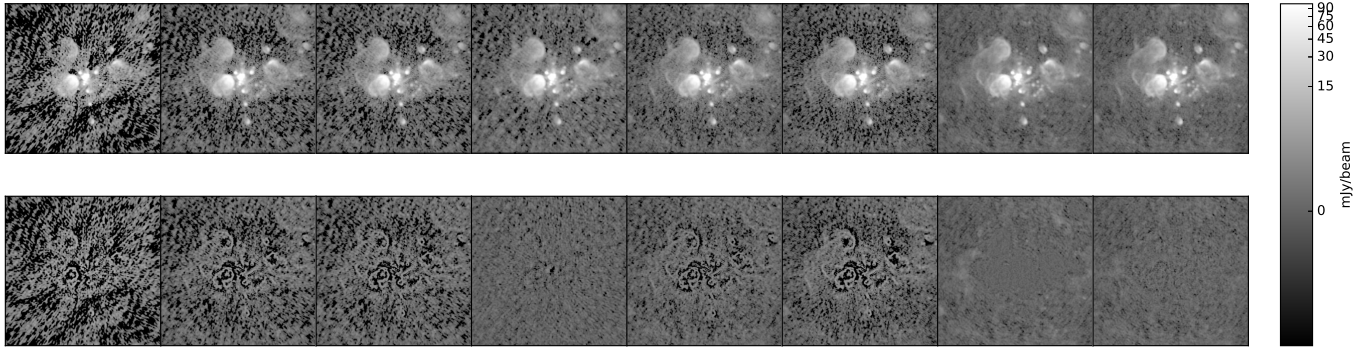


Figure 17. Progression of the self-calibration iterations. The images show, from left to right, the initial image, one, two, and three iterations of phase-only self calibration, two iterations of phase and amplitude self-calibration, a reimaging of the 5th iteration with a deeper 0.1 mJy threshold using a mask at the 2.5 mJy level, and finally, a sixth iteration of phase and amplitude self-cal cleaned to 0.1 mJy over a region thresholded at 1.5 mJy. All imaging was done using two Taylor terms and multiscale clean. The second row shows the corresponding residual images.

For sources with $T_{B,max} > 40$ K, it is not possible to measure a mass assuming $T = 40$ K, so those entries are left empty.

Table 3. Continuum Source IDs and photometry

ID	Cluster	Classification	Coordinates	$S_{\nu,max}$	$T_{B,max}$	$S_{\nu,tot}$	σ_{bg}	α	$E(\alpha)$	M_{40K}	$N(\text{H}_2)_{40K}$
				mJy bm^{-1}	K	mJy	mJy bm^{-1}			M_\odot	cm $^{-2}$
174 f3	M	S_ HII	17:47:20.167 -28:23:04.809	1600	860	2400	46	0.89	0.002	-	-
234 f4	M	S_ HII	17:47:20.214 -28:23:04.379	1100	570	900	23	0.83	0.001	-	-
176 f1	M	S_ denseCore	17:47:20.127 -28:23:04.082	920	480	1400	30	1.2	0.006	-	-
236 f10.303	M	S_ HII	17:47:20.106 -28:23:03.729	890	460	800	19	1.1	0.015	-	-
235 f2	M	S_ HII	17:47:20.166 -28:23:03.714	820	430	670	33	1.3	0.002	-	-
172 K2	N	S_ denseCore	17:47:19.869 -28:22:18.466	370	200	650	49	2.5	0.018	-	-
175 G	M	S_ HII	17:47:20.285 -28:23:03.162	340	180	390	5.6	0.68	0.03	-	-
237 G10.44	M	S_ HII	17:47:20.241 -28:23:03.387	280	140	160	15	0.69	0.006	-	-
178 f10.37	M	SX_ HII	17:47:20.178 -28:23:06	200	100	270	18	1.5	0.039	-	-
171 K3	N	S_ HII	17:47:19.895 -28:22:17.221	190	97	280	25	1.4	0.023	-	-
177 B	M	S_ HII	17:47:19.918 -28:23:03.039	150	77	240	3.9	0.47	0.011	-	-
241	M	S_ denseCore	17:47:20.106 -28:23:03.066	140	73	120	15	1.4	0.05	-	-
179 f10.38	M	S_ HII	17:47:20.193 -28:23:06.673	130	66	180	9.3	1.6	0.013	-	-
180 E	M	S_ HII	17:47:20.108 -28:23:08.894	130	66	190	4	0.38	0.014	-	-
173 K1	N	S_ HII	17:47:19.78 -28:22:20.743	92	48	150	4.4	0.58	0.034	-	-
170	N	S_ PartofCloud	17:47:19.895 -28:22:13.621	92	48	160	23	1.7	0.082	-	-
252	N	S_ denseCore	17:47:19.862 -28:22:13.168	82	43	160	15	1.9	0.078	-	-
225 f10.33b	M	SX_ denseCore	17:47:20.116 -28:23:06.374	69	36	100	14	1.9	0.21	1200	3.6×10^{26}
96 Z10.24	-	S_M Maser	17:47:20.039 -28:22:41.25	64	33	75	1.5	0.68	0.37	1100	2.5×10^{26}
181 D	M	S_M HII	17:47:20.051 -28:23:12.91	59	31	94	1.3	0.64	0.088	990	2×10^{26}
240 f10.44b	M	S_ HII	17:47:20.252 -28:23:06.463	57	30	51	11	1.8	0.015	960	1.8×10^{26}
233 f10.27b	M	S_ HII	17:47:20.077 -28:23:05.383	50	26	78	18	2.3	0.18	840	1.4×10^{26}
239	M	S_ denseCore	17:47:20.242 -28:23:07.222	45	24	46	8.6	2.3	0.091	760	1.1×10^{26}
244 C	M	S_ -	17:47:19.981 -28:23:18.437	35	19	67	0.49	0.47	0.081	600	7.8×10^{25}
242	M	S_ denseCore	17:47:20.129 -28:23:02.247	32	17	63	8.5	2.2	0.099	540	6.8×10^{25}
92 I10.52	M	S_ HII	17:47:20.324 -28:23:08.2	32	17	45	5.3	0.63	0.061	530	6.6×10^{25}
245 A2	-	S_ -	17:47:19.562 -28:22:55.916	25	13	32	2.1	0.54	0.025	410	4.8×10^{25}
109	N	S_ -	17:47:19.901 -28:22:15.54	24	13	41	13	3.6	0.3	410	4.7×10^{25}
87 B9.99	M	S_ HII	17:47:19.798 -28:23:06.942	23	12	37	1.9	0.89	0.042	390	4.4×10^{25}
88	M	S_ -	17:47:19.617 -28:23:08.26	23	12	34	2.9	3.1	0.18	380	4.3×10^{25}
151 B10.06	M	S_M HII	17:47:19.86 -28:23:01.5	21	11	31	1.3	0.19	0.79	350	3.8×10^{25}
98	-	S_M Maser	17:47:19.53 -28:22:32.55	18	9.5	29	0.36	3.2	1.1	300	3.3×10^{25}
152 f10.32	M	S_ HII	17:47:20.128 -28:23:00.22	16	8.5	27	3	-0.3	0.26	270	2.9×10^{25}
86 B9.96	M	S_ HII	17:47:19.766 -28:23:10.183	16	8.3	24	1.8	1	0.089	270	2.9×10^{25}

The Classification column consists of three letter codes as described in Section 3.2. In column 1, S indicates a strong source, W indicates weak or low-confidence source. In column 2, an X indicates a match with the [Muno et al. \(2009\)](#) Chandra X-ray source catalog, while an underscore indicates there was no match. In column 3, M indicates a match with the, [Caswell et al. \(2010\)](#) Methanol Multibeam Survey CH₃OH maser catalog, while an underscore indicates there was no match. Finally, we include the SIMBAD ([Wenger et al. 2000](#)) source object type classification if one was found.